Enhancing the mechanical strength of β-Ga_2O_3 with Al alloying

Yuchao Yan,[1,2] Cheng Li,[2,3] Ning Xia,[3] Tianqi Deng,[1,2,*] Hui Zhang,[1,2,†] and Deren Yang[1,2]

[1] *State Key Laboratory of Silicon and Advanced Semiconductor Materials and School of Materials Science and Engineering, Zhejiang University, Hangzhou, Zhejiang 310027, China*

[2] *Institute of Advanced Semiconductors & Zhejiang Provincial Key Laboratory of Power Semiconductor Materials and Devices, Hangzhou Global Scientific and Technological Innovation Center, Zhejiang University, Hangzhou, Zhejiang 311200, China*

[3] *Hangzhou Garen Semiconductor Company Limited, Hangzhou, Zhejiang 311200, China*

(Received 30 October 2023; revised 10 April 2024; accepted 22 May 2024; published 14 June 2024)

β-Ga_2O_3 is a promising ultrawide-bandgap semiconductor material for power electronics and optical applications. However, its low hardness and cleavage nature pose major challenges to crystal growth and processing. In this study, Al alloying is proposed as an effective method to improve the mechanical properties of β-Ga_2O_3 as seed crystals and substrates. First-principle calculations are employed to assess the alloying-induced evolution of crystal structure and mechanical behavior. Elastic constants, ideal shear strengths, and ideal cleavage strengths are all shown to enhance with increasing Al concentration. Our analysis reveals the possibility of obtaining the mechanically favorable β-Ga_2O_3 seed crystals and substrates with proper Al alloying, providing theoretical guidance to the development of β-Ga_2O_3 materials and devices.

DOI: 10.1103/PhysRevApplied.21.064036

I. INTRODUCTION

β-Ga_2O_3 is a promising semiconductor material with an ultrawide bandgap (around 4.8 eV) [1]. The high breakdown field [2,3], high Baliga's figure of merit [4,5], and high thermal and chemical stability [6–8] of β-Ga_2O_3 warrant its application in high-performance electronic and optical devices. Large-scale single crystal substrates up to six inches can be synthesized through the Czochralski method [9,10], edge-define film-fed growth [11,12], vertical Bridgeman [13], and a recently developed casting method [14]. Compared with SiC and GaN, the molten growth techniques remarkably expand the accessibility to low-cost, large-scale, and dislocation-free β-Ga_2O_3 substrates, which will facilitate the prosperity of its power devices in the upcoming decades.

Industrial scale manufacturing of β-Ga_2O_3 substrates requires complex yet precise bulk crystal growth and ingot processing, where the mechanical properties play the decisive role. Unlike SiC and GaN, with hardnesses of 42 GPa [15] and 16 GPa [16], respectively, β-Ga_2O_3 is a relatively soft semiconductor material. Due to the soft and cleaving nature of β-Ga_2O_3, the seed crystals for molten growth and the processed substrates are susceptible to deformation and cracking, making it difficult to obtain a high product yield. Furthermore, heat accumulation in seed crystal during near-melting-point growth of β-Ga_2O_3 tends to melt itself due to the ultralow thermal conductivity of β-Ga_2O_3 of 0.27 $W \cdot cm^{-1} \cdot K^{-1}$ [17], thus interfering with the growth process. Consequently, the optimization of elastic properties, deformation behavior, and cleavage strength of β-Ga_2O_3 and its seed crystal is of great importance to the β-Ga_2O_3 industry.

Many attempts have been made to explore the mechanical properties of β-Ga_2O_3, both experimentally and theoretically [18–23]. Due to the low-symmetry monoclinic crystal lattice and distorted microstructure of β-Ga_2O_3, the measured mechanical strength of β-Ga_2O_3 exhibits a strong anisotropy. Gao *et al.* [22] conducted a systematic investigation of the fracture and deformation mechanism of β-Ga_2O_3. The (010)-plane showed a relatively small elastic modulus $E = 176.7 \pm 2.88$ GPa and a low hardness of 6.8 ± 0.35 GPa, which was attributed to the strong ionicity of chemical bonds and tiling stacking structure of the (010)-plane. In general, the arrangements of atoms and bonds are the origins of the mechanical properties of β-Ga_2O_3.

Alloying is an important technique for modulating and optimizing semiconductor properties. Al_2O_3 is a promising β-Ga_2O_3-alloying candidate due to its ultrawide bandgap of 8.2 eV and the identical valence electron configuration of Al and Ga [24]. Mizuno *et al.* [25] experimentally measured the phase diagram of Al_2O_3-Ga_2O_3. The

*Corresponding author: dengtq@zju.edu.cn
†Corresponding author: msezhanghui@zju.edu.cn

liquidus of β-$(Al_xGa_{1-x})_2O_3$ rises with increasing Al concentration, which may be effective in preventing the seed crystal from melting during molten growth processes. The most comprehensive investigations on the bulk growth of β-$(Al_xGa_{1-x})_2O_3$ were conducted by Galazaka *et al.* by growing various β-$(Al_xGa_{1-x})_2O_3$ samples of 20 mm in diameter with Al contents from 0 to 30 mol % through the Czochralski method [10]. The lattice constants of the alloyed crystals decrease linearly with increasing Al concentration, while the crystal growth was stable up to a 30% Al concentration in the melt. In addition to the experiments, density functional theory (DFT) calculations were carried out by Peelaers *et al.* to investigate Al substitution and phase stability of the β-$(Al_xGa_{1-x})_2O_3$ alloys [26]. It was revealed that Al atoms preferentially substitute the octahedral Ga sites of β-Ga_2O_3 before the tetrahedral sites, and the monoclinic phase is stable up to 75% Al content. In the field of epitaxy growth, molecular beam epitaxy (MBE) [27], metalorganic chemical vapor deposition (MOCVD) [28], and pulsed laser deposition (PLD) [29] have been utilized to grow high-quality β-$(Al_xGa_{1-x})_2O_3$ films. Taken together, homogeneous alloys of β-$(Al_xGa_{1-x})_2O_3$ have been successfully synthesized in both bulk and film, which inspires the mechanical property investigation of β-$(Al_xGa_{1-x})_2O_3$ for future applications.

In this study, Al alloying effect on the mechanical strength of β-Ga_2O_3 is investigated from first principles with Al molar content up to 50%. Alloying-induced evolutions of lattice structure, elastic constants, ideal shear strength, and ideal cleavage strength are analyzed. A 20% increase of minimum Young's modulus and shear modulus, a 56.3% increase of ideal shear strength along the (001)/⟨010⟩ slip system, a 22% increase of the ideal cleavage strength of the (100)-B plane, and a 16% increase of the ideal cleavage strength of the (001)-B plane are observed upon 50% Al alloying. These observations indicate that β-$(Al_xGa_{1-x})_2O_3$ is mechanically enhanced for applications as seed crystals in molten growth and substrates for epitaxy GaN. The bond stiffening arising from Al alloying was revealed as the microscopic origin of mechanical strength enhancement. Our analysis indicates the possibility of obtaining mechanically favorable β-Ga_2O_3 seed crystals and substrates with proper Al alloying, providing theoretical guidance for the development of β-Ga_2O_3 material and devices.

II. RESULTS AND DISCUSSION

A. Crystal structure

The monoclinic crystal structure of β-Ga_2O_3 has a $C2/m$ space group. As shown in Fig. 1, the unit cell of β-Ga_2O_3 has two crystallographically inequivalent gallium sites and three inequivalent oxygen sites, denoted as GaI and Ga_{II} and O_I, O_{II}, and O_{III}, respectively. The Ga_I atoms reside

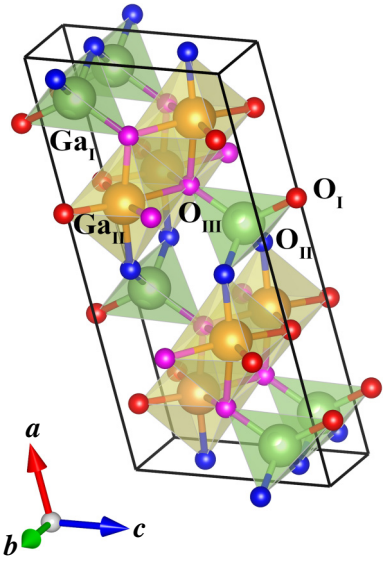

FIG. 1. Conventional unit cell of β-Ga_2O_3. Here, O_I, O_{II}, O_{III}, Ga_I, and Ga_{II} are represented by red, blue, pink, green, and brown spheres, respectively. The octahedron consists of three O_{III}, two O_I, one O_{II}, and one Ga_{II}. The tetrahedron consists of two O_{II}, one O_{III} and O_I, and one Ga_I.

within the Ga-O tetrahedrons and the Ga_{II} atoms inhabit the octahedrons. The O_I and O_{II} sites are tricoordinated and the O_{III} sites are tetracoordinated. The DFT calculation of the mechanical properties requires reliable lattice parameters and PBEsol functional provides an accurate prediction of $a = 12.26$ Å, $b = 3.05$ Å, $c = 5.82$ Å, and $\beta = 103.8°$ [30,31]. The DFT calculation details are discussed in Appendix A. This result is in good accordance with experimental parameters of $a = 12.23$ Å, $b = 3.04$ Å, $c = 5.80$ Å, and $\beta = 103.7°$ [32]. The length of the tetrahedral Ga_I atom bonds with O_I (1.839 Å), O_{II}(1.842 Å), and O_{III}(1.873 Å) and the octahedral Ga_{II} atom bonds with O_I(1.948 Å), O_{II}(1.942 Å), and O_{III}(2.012 Å for short bonds and 2.084 Å for long bonds) were calculated. As seen from the bond lengths, the tetrahedral sites of β-Ga_2O_3 are slightly distorted. In contrast, the octahedral sites are highly distorted, which enhances the mechanical anisotropy arising from its low-symmetry structure. One can, therefore, expect low strengths along the shear and tension directions of the longest and weakest Ga_{II}—O_{III} (2.084 Å) bonds and high strengths along the shear and tension directions of the shortest and strongest Ga_I—O_I (1.839 Å) bonds. The above bond calculations are also in good accordance with experimental studies [32].

The mechanical properties of β-$(Al_xGa_{1-x})_2O_3$ alloys are modeled with special quasirandom structures (SQS) constructed by the cluster expansion method implemented in an alloy theoretic automated toolkit (ATAT). Our Monte Carlo simulations demonstrated that Al prefers to randomly substitute Ga_{II} sites in β-$(Al_xGa_{1-x})_2O_3$ alloys with $0 < x < 0.5$. While the maximum Al concentration for bulk

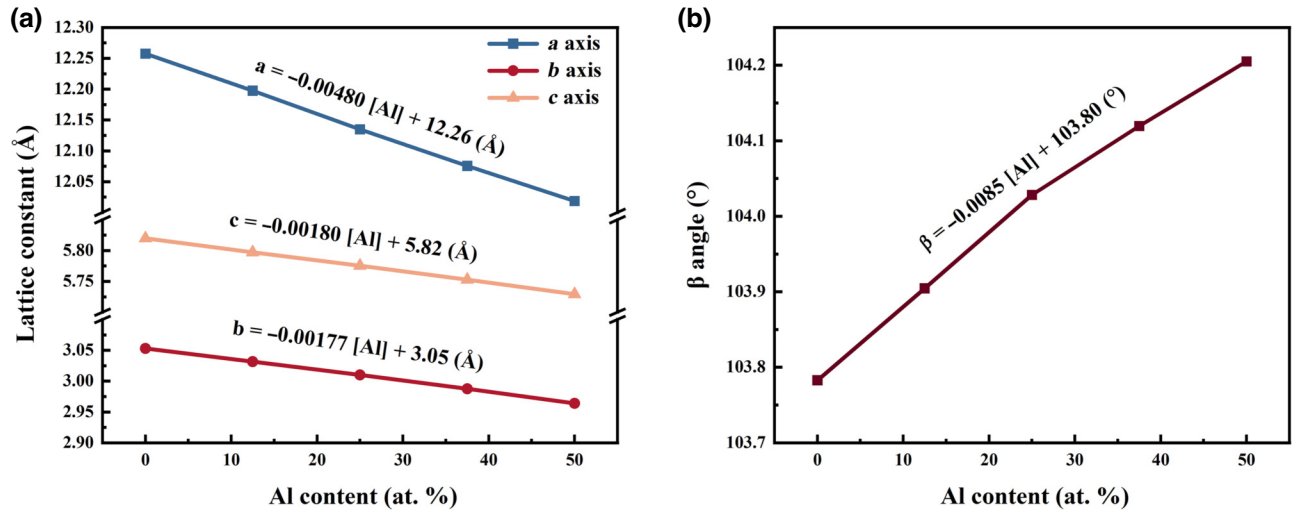

FIG. 2. (a) Lattice constants a, b, and c axis and (b) β angle versus Al concentration from 0 to 50 at. %.

growth is 25 at. % due to phase separation, epitaxial films with higher Al concentrations of up to 52 at. % have been fabricated by Bhuiyan *et al*. utilizing the MOCVD method on the (100)- and (−201)-substrates [28,33]. Thus, the Ga_{II} sites in the alloyed structures were reasonably substituted by Al atoms up to 50% molar content, while the Ga_I sites remained unsubstituted. A detailed discussion on the Al substitution can be found in Appendix B. The Al alloying effect on lattice constants is shown in Fig. 2. All lattice vector lengths decrease linearly with increasing Al concentration in β-Ga_2O_3. The slopes of a, b, and c axes are −0.00480 Å/at. %, −0.00177 Å/at. %, and −0.00180 Å/at. %, respectively, and the slope of β angle is 0.0085°/at. %, which are in good accordance with Galzaka's experimental works on bulk growth [9].

Such lattice contraction is beneficial for the heteroepitaxy of (0001)-plane GaN on (100)-plane β-Ga_2O_3. Villora *et al*. experimentally determined the in-plane epitaxy relationship between GaN and β-Ga_2O_3 as Ga_2O_3 $\langle 010\rangle$ || GaN $\langle 11\bar{2}0\rangle$ and Ga_2O_3 $\langle 001\rangle$ || GaN $\langle 1\bar{1}00\rangle$ [34]. As shown in Fig. 3(a), the Ga atoms in the (100)-plane of β-Ga_2O_3 are arranged in a quasihexagonal structure with the $\langle 011\rangle$-direction as the diagonal. The lattice length of the $\langle 011\rangle$-direction of β-Ga_2O_3 is 6.57197 Å according to the aforementioned calculations. The lattice constants of GaN are $a = 3.19091$ Å and $c = 5.18796$ Å [35], and the hexagonal structure is shown in Fig. 3(b) with diagonal $\langle 2\bar{1}\bar{1}0\rangle$ lattice = 6.38182 Å. Consequently, the lattice mismatch between GaN $\langle 2\bar{1}\bar{1}0\rangle$-direction and β-Ga_2O_3 $\langle 011\rangle$-direction is derived as 2.89%, which is in good accordance with Villora's experimental works. As Al alloying introduces a linear contraction on lattice constants of β-$(Al_xGa_{1-x})_2O_3$ with increasing concentration, the lattice mismatch between β-$(Al_xGa_{1-x})_2O_3$ and GaN also linearly decreases to 1.1% at $x = 0.5$. Compared with the lattice mismatch between sapphire and GaN (∼16%) [36] and SiC and GaN (∼3.8%) [37], β-$(Al_xGa_{1-x})_2O_3$ substrates are more favorable for growing high-quality GaN epitaxy layers. In consideration of the high cost of homoepitaxy on GaN substrates, the low-cost β-$(Al_xGa_{1-x})_2O_3$

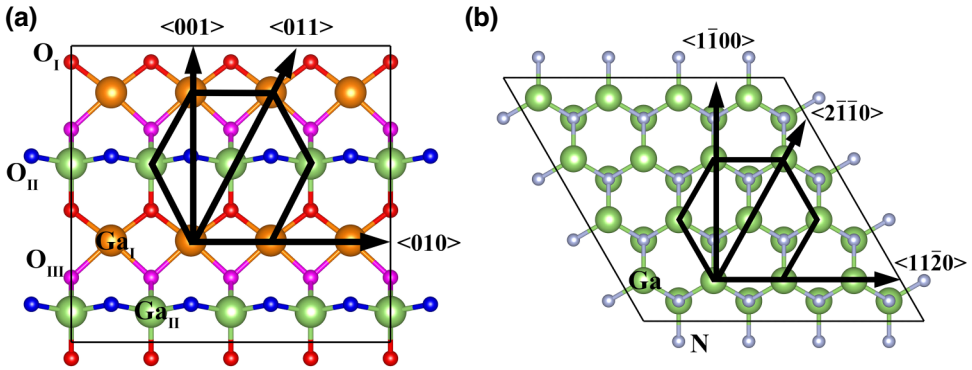

FIG. 3. In-plane lattice relationship of (a) Ga_2O_3 (100)-plane and (b) GaN (0001)-plane. The epitaxy relationships are Ga_2O_3 $\langle 010\rangle$ || GaN $\langle 11\bar{2}0\rangle$ and Ga_2O_3 $\langle 001\rangle$ || GaN $\langle 1\bar{1}00\rangle$.

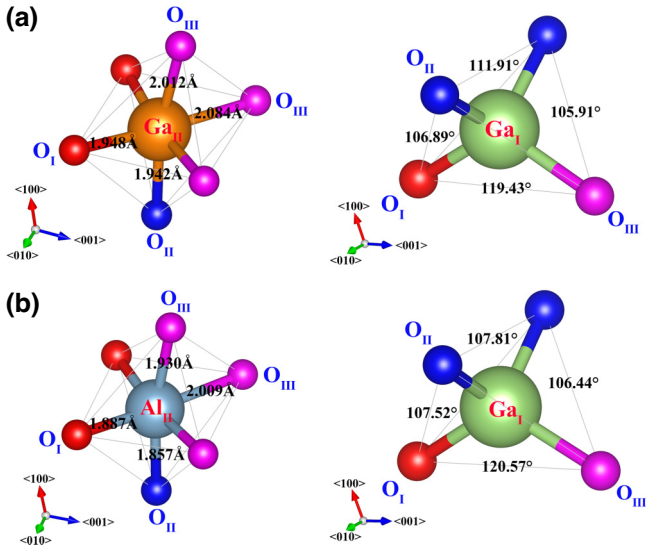

FIG. 4. Octahedral (left) and tetrahedral (right) sites of (a) β-Ga_2O_3 and (b) β-$Al_{II}Ga_IO_3$. The bond distances of the octahedron and the bond angles of tetrahedrons are labeled.

substrates from molten growth techniques will be the better choice.

Apart from lattice constants, Al alloying also introduces bond stiffening with microscopic strain to the crystal structure of β-Ga_2O_3. Figure 4 shows the distorted tetrahedron and octahedron coordinates of β-Ga_2O_3 and β-$Al_{II}Ga_IO_3$, i.e., the ordered β-$(Al_{0.5}Ga_{0.5})_2O_3$ alloy with Ga_{II} sites completely substituted by Al. The bond lengths around the octahedral sites change significantly after Al substitution. The O_{II} bonds in the octahedrons undergo the largest decrease of 0.085 Å while the O_I bonds reduce by a relatively small amount of 0.061 Å, indicating atomic scale strains introduced by alloying. In contrast, no significant change is observed in the bond lengths of the tetrahedral sites. However, the small stretching and compression of each bond indicate a small compressive strain along the O_I and O_{II} directions of tetrahedrons and a tensile strain along O_{III}. Such evolution mainly stems from the strain introduced by Al substituting octahedral sites. The bond angles of the tetrahedral sites are significantly affected by such strain. As shown in Fig. 4, the bond angles are 105.91° (O_{III}—Ga_I—O_{II}), 106.89° (O_I—Ga_I—O_{II}), 111.91° (O_{II}—Ga_I—O_{II}), and 119.43° (O_{III}—Ga_I—O_I). Upon 50 at. % Al alloying, the O_{III}—Ga_I—O_I angle increases slightly to 120.57°, while O_{II}—Ga_I—O_{II} angle significantly decreases by 4.1° to 107.81°. The O_{III}—Ga_I—O_{II} and O_I—Ga_I—O_{II} angles also slightly increase to 106.44° and 107.52°, respectively. The differences among O_{III}—Ga_I—O_{II}, O_I—Ga_I—O_{II}, and O_{II}—Ga_I—O_{II} angles are reduced, which means the tetrahedral sites become less distorted. These bond length and bond angle variations can be regarded as the origins of the larger lattice shrinkage along the ⟨010⟩-axis compared with the ⟨100⟩- and ⟨001⟩-axes.

To assess the bond-stiffening effect introduced by Al alloying, traces of interatomic force constant (IFC) tensors of β-Ga_2O_3 and β-$Al_{II}Ga_IO_3$ are calculated and summarized in Fig. 5(a) (see Appendix C for the IFC calculation methods). The IFC, as a microscopic analog to the spring constant, is a suitable measure for bond stiffness. Within β-Ga_2O_3, the Ga_{II}-O_I bond possesses the largest IFC while the value of Ga_{II}—O_{III}(long) bonds is approximately one-third of it, signifying the strength difference between short Ga_I—O_I bonds and long Ga_{II}—O_{III} bonds. Upon Al alloying, the IFC of all the bonds in β-$Al_{II}Ga_IO_3$ are enhanced compared with β-Ga_2O_3, and the Al_{II}—O_{II}

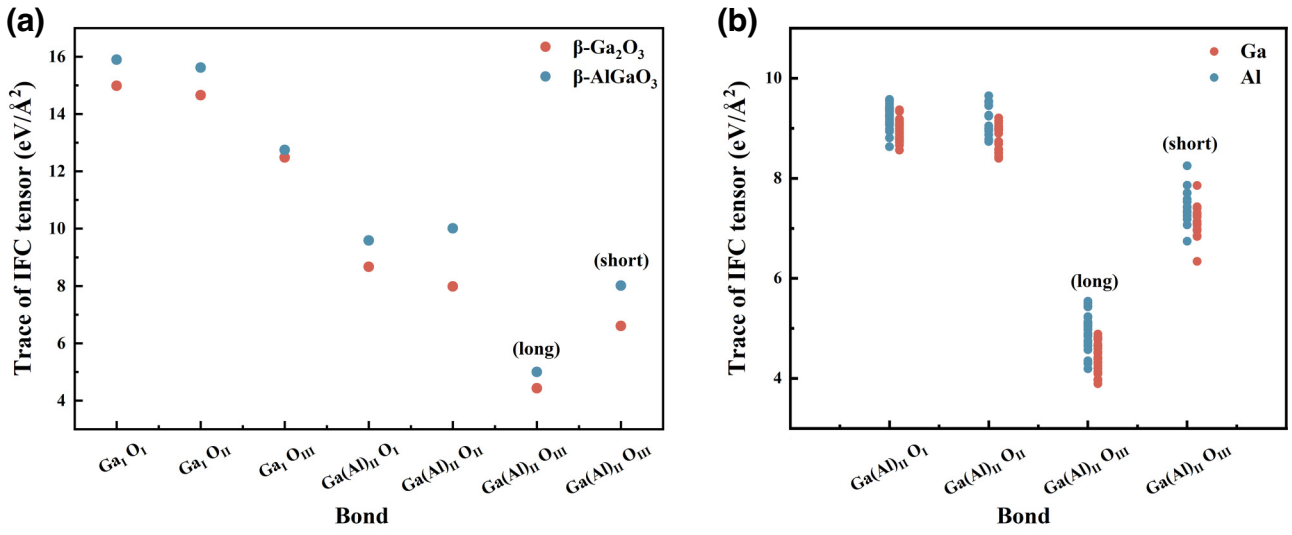

FIG. 5. Trace of interatomic force constant tensors between Ga/Al and their neighboring O in (a) β-Ga_2O_3 and β-$Al_{II}Ga_IO_3$ and (b) β-$Al_{0.5}Ga_{1.5}O_3$.

TABLE I. Summarization of the elastic constants of β-Ga_2O_3.

Method	Elastic constants (GPa)												
	C_{11}	C_{22}	C_{33}	C_{44}	C_{55}	C_{66}	C_{12}	C_{13}	C_{23}	C_{15}	C_{25}	C_{35}	C_{46}
Experiment [18]	240.7	349.1	345.0	48.1	87.9	103.5	128.2	160.4	72.0	−1.68	0.36	0.97	5.89
PBE [19]	206.2	324.2	297.1	39.8	83.8	97.2	124.1	123.2	63.4	−2.98	−0.41	13.9	4.67
AM05 [38]	223.1	333.2	330.0	50.3	68.6	94.2	116.5	125.3	75.0	−17.4	12.2	7.3	17.4
PBEsol (This work)	220.6	332.5	330.1	50.9	65.6	93.7	115.7	128.4	77.6	−17.0	12.0	6.6	17.5

bonds exhibit the largest increase compared with Ga_{II}—O_{II} bonds. Notably, there is an increase in bond strength even for the unsubstituted Ga_I tetrahedron, indicating the integral role of Al atoms in the overall bond stiffening of β-$Al_{II}Ga_IO_3$. To attain further insights, the traces of the IFC tensors for bonds around octahedral sites in random β-$Al_{0.5}Ga_{1.5}O_3$ alloy are also calculated and shown in Fig. 5(b). An overall stronger bond strength of Al_{II} sites over Ga_{II} sites is clearly observed, again signifying the bond-stiffening effect of Al substitution.

B. Elastic constants

To investigate the mechanical properties of β-$(Al_xGa_{1-x})_2O_3$ alloys, we utilized the stress-strain method to evaluate the elastic constants as well as the derived properties. The material β-Ga_2O_3 belongs to the monoclinic system and has 13 independent elastic tensor components, which are summarized in Table I. The β-Ga_2O_3 data in this work agrees with previous experimental and calculation works [18,19,38]. The elastic properties of β-Ga_2O_3 are highly anisotropic due to the low-symmetry monoclinic crystal lattice. Using the Voigt-Resus-Hill method, the anisotropic and isotropic bulk modulus, B, Young's modulus, E, and shear modulus, G, of β-Ga_2O_3 can be derived [39]. The isotropic $B = 168.2$ GPa, $E = 192.4$ GPa, and $G = 73$ GPa are in good accordance with the experimental results [18]. In terms of anisotropic properties, the minimum $B = 119.61$ GPa, $E = 122.72$ GPa, and $G = 44.67$ GPa indicate that β-Ga_2O_3 is a relatively soft semiconductor material that is susceptible to external forces. Furthermore, the maximum $B = 216.58$ GPa, $E = 275.76$ GPa, and $G = 126.584$ GPa differ significantly from the minimums, further showing the highly anisotropic mechanical properties of β-Ga_2O_3.

The maximum, minimum, and isotropy Young's modulus E and shear modulus G of β-$(Al_xGa_{1-x})_2O_3$ alloys are calculated and visualized in Fig. 6. All moduli are apparently enhanced with increased Al concentration. The minimum E increases by 20% from 122.72 GPa (Al = 0 at. %) to 146.75 GPa (Al = 50 at. %) and the minimum G also increases by 20% from 44.67 GPa (Al = 0 at. %) to 53.54 GPa (Al = 50 at. %), indicating a strong hardening effect of Al alloying.

Based on the elastic constants, various models have been developed to predict the critical failure mechanism of a certain material. Here, we employ Pugh's ratio, P_r, and Cauchy pressure, C_p, as the ductile and brittle failure measurements [40]. The standard definitions of these two parameters are as follows:

$$P_r = \frac{B_v}{G_v}, \tag{1}$$

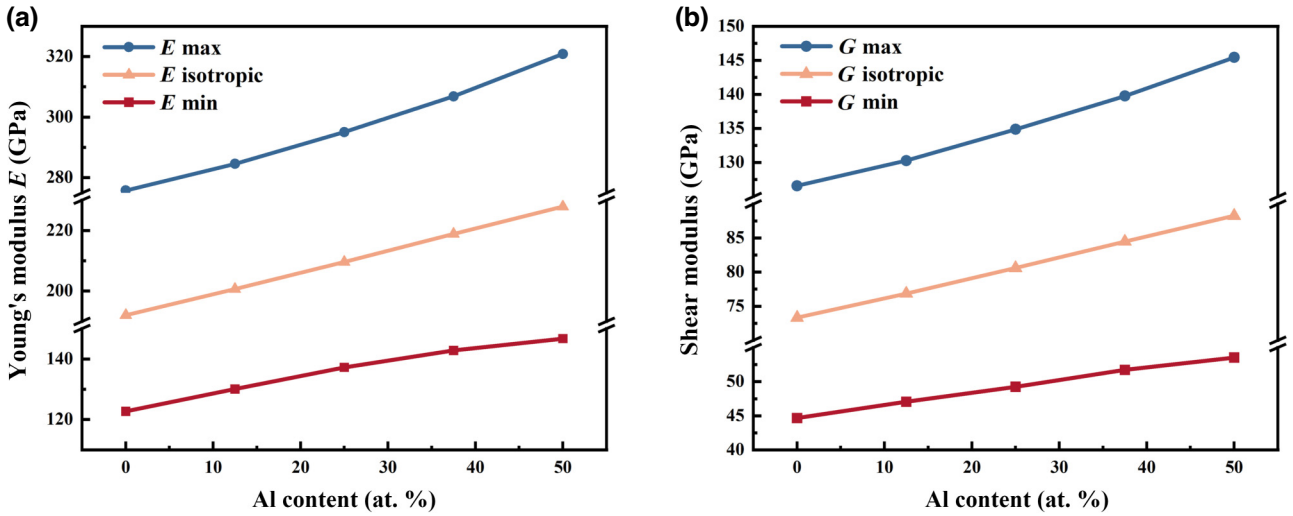

FIG. 6. Minimum, maximum, and average of (a) Young's modulus and (b) shear modulus.

$$C_{\mathrm{p}} = B\left(1 - \frac{5G_v}{3B_v}\right), \tag{2}$$

where G_v and B_v are the shear modulus and bulk modulus in Voigt notation. In monoclinic systems like β-Ga_2O_3, the G_v and B_v can be expressed as:

$$G_v = \frac{(C_{44} + C_{55} + C_{66}) + (C_{11} + C_{22} + C_{33}) - (C_{12} + C_{13} + C_{23})}{5}, \tag{3}$$

$$B_v = \frac{(C_{11} + C_{22} + C_{33}) + 2(C_{12} + C_{13} + C_{23})}{9}. \tag{4}$$

The value of Pugh's ratio is a quantitative criterion describing the possible failure mechanism of a material. Specifically, the failure mechanisms of metals demonstrate a transition from brittle failure to ductile failure when the value of Pugh's ratio increases, where the value of 1.75 is regarded as the boundary [40]. However, the criterion for Pugh's ratio is empirical and has not been well-established for semiconductors. Thus, there is no established, definitive numerical distinction between ductile and brittle failure mechanisms of semiconductors. Nevertheless, they can still provide the trend of the possible failure mechanisms of the alloys studied here. The calculated Pugh's ratios are plotted in Fig. 7. The decrease indicates that, with Al alloying, β-Ga_2O_3 moves further away from the ductile failure and into the brittle failure region. It should be noted that this is not a quantification of the materials' failure mechanism. Instead, experiments are required to take into consideration the plastic flow and fracture process. Apart from Pugh's ratio, the value of Cauchy pressure is also a quantitative criterion measuring the resistance to the external force of a certain material. Material with higher resistance to external force possesses a smaller Cauchy pressure and vice versa [40]. The values of Cauchy pressure of the alloys studied here are also visualized in Fig. 7. Identical to Pugh's ratio, the value of Cauchy pressure exhibits an obvious decline with increasing Al concentration, indicating the strengthening effect of Al alloying.

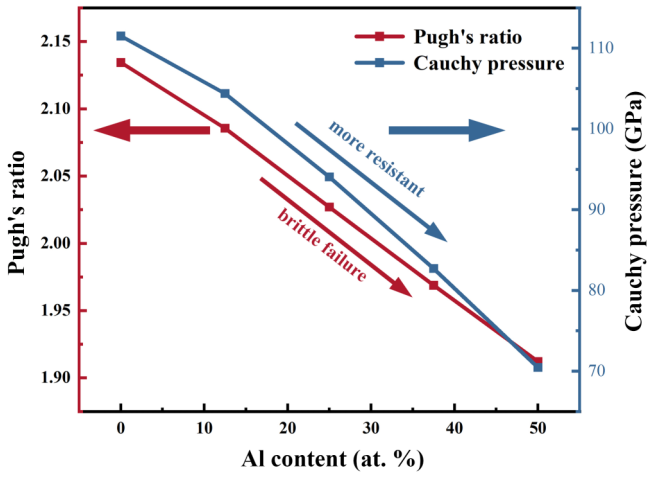

FIG. 7. Pugh's ratio and Cauchy pressure versus Al concentration.

Taken together, the elastic properties of β-Ga_2O_3 are highly anisotropic due to its low symmetry and distorted microstructure. With Al alloying that introduces bond stiffening, the minimum Young's modulus and shear modulus of β-$(Al_xGa_{1-x})_2O_3$ are increased. Analyses of Pugh's ratio and Cauchy pressure indicate that, with increasing Al concentration, it is less likely for β-$(Al_xGa_{1-x})_2O_3$ to experience ductile failure.

C. Ideal shear strength

Ideal shear strength is defined as the critical shear stress a material can endure without permanent plastic deformation. It is an intrinsic property determined by the bonding nature and structure of a crystal, and the defect-free ideal shear strength can be predicted by first-principle calculations [41–44]. The value of the ideal shear strength has been widely utilized to explore the deformation and fracture behavior of metals and their alloys. A previous study has primarily investigated the shear-induced mechanical failure of β-Ga_2O_3 under ideal shear and indentation stress conditions [45].

To investigate the most deformable and easiest slip system for comparison, affine shear deformations were performed in two low index planes along different directions, i.e., (001)/⟨010⟩, (001)/⟨100⟩, and (100)/⟨010⟩ slip systems. Figure 8(a) shows the calculated shear-stress-strain curves with a strain interval of 0.01. Fine searches are performed around the critical shear stress with a strain interval of 0.001 in order to obtain detailed information on the deformed structure. The calculated shear moduli are 4.8 GPa along (001)/⟨010⟩, 6.3 GPa along (001)/⟨100⟩, and 9.8 GPa along (100)/⟨010⟩, respectively. The C_{ij} calculation of β-Ga_2O_3 indicates a minimum shear modulus of 4.5 GPa, with a first minimum direction along

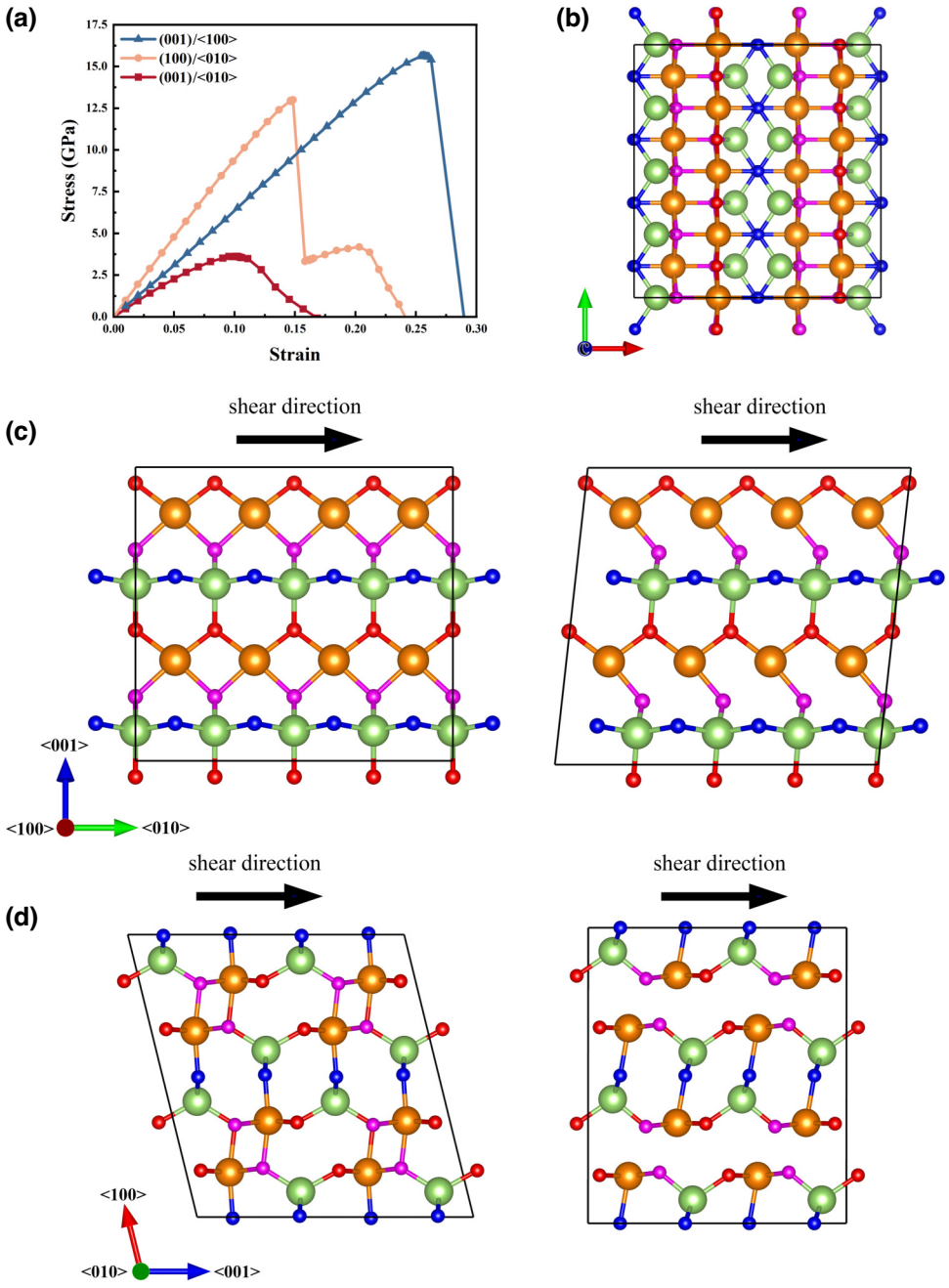

FIG. 8. (a) Ideal shear strengths of β-Ga_2O_3 along the (001)/⟨010⟩, (001)/⟨100⟩, and (100)/⟨010⟩ slip systems; (b) unsheared structure projected along the ⟨001⟩-axis; (c) unsheared (left) and sheared (right) structure of the (001)/⟨010⟩ slip system projected along the ⟨100⟩-axis; (d) unsheared (left) and sheared (right) structure of the (001)/⟨100⟩ slip system projected along the ⟨010⟩-axis.

(−0.336, 0.000, 0.9418) and the second minimum direction along (0.000, −1.000, 0.000). By comparing with C_{ij}, we found that the (001)/⟨010⟩ possesses a near-minimum shear modulus. As for the ideal shear strength, the minimum is 3.6 GPa along (001)/⟨010⟩, significantly weaker than the 13.0 GPa along (100)/⟨010⟩ and the 15.7 GPa along (001)/⟨100⟩. Thus, the (001)/⟨010⟩ can serve as the representative of the weakest slip system of β-Ga_2O_3. Details of the ideal shear strength calculations are further discussed in Appendix D.

During pure shear deformation of β-Ga_2O_3, bond breaking serves as the decisive failure factor. The crystalline structures with shear deformation along (001)/⟨010⟩ are shown in Fig. 8(c). Upon pure shear, the Ga_{II}-O_{III} bonds are stretched, contributing to the corresponding shear stress, which reaches its maximum at 0.102 strain. Beyond

the critical strain, the Ga_{II}—O_{III}(long) bonds are stretched to 2.458 Å at 0.122 strain, and the corresponding stress declines by 1.2 GPa. Thus, the Ga_{II}—O_{III}(long) bond breaking is the underlying mechanism for the ideal shear strength of the (001)/⟨010⟩ slip system. Compared with the other two slip systems, the shear failure of (001)/⟨010⟩ is much more ductile, i.e., the dwell strain around the ideal shear point is much larger than the others. Such a result can be attributed to the distinct bond arrangements along different crystal directions due to the low-symmetry structure of β-Ga_2O_3. The shear mechanism along (001)/⟨100⟩ is shown in Fig. 8(d). Similar to (001)/⟨010⟩, the overstretching of Ga_{II}—O_{III} (short) bonds leads to irreversible plastic deformation, resulting in a much higher ideal shear strength. The ideal shear strength of (100)/⟨010⟩ is complicated due to the densely packed bonds and atoms along ⟨100⟩, as shown in Fig. 8(b). The atomic structures and bond length evolution during pure shear deformation are shown in detail in Appendix D. When strain exceeds the critical limit, a significantly large shear component σ_4 of around 0.3 emerges, and the crystal structure is subjected to an irreversible deformation. Taken together, bond stretching and breaking serve as the decisive factors in the pure shear deformation process of β-Ga_2O_3 along various slip systems.

The shear-stress-strain curves of β-$(Al_xGa_{1-x})_2O_3$ alloy along (001)/⟨010⟩ are shown in Fig. 9(a). Upon Al alloying, the ideal shear strain increases from 0.102 (Al = 0 at. %) to 0.121 (Al = 50 at. %), i.e., by 19%, and the ideal shear stress increases from 3.63 GPa (Al = 0 at. %) to 5.67 GPa (Al = 50 at. %), i.e., by 56.3%. However, the relatively ductile shear behavior remains independent of Al alloying. Taking β-$Al_{II}Ga_IO_3$ as a comparison, the Al_{II}—O_{III} bonds in β-$Al_{II}Ga_IO_3$ are stretched from 2.009 to 2.212 Å at 0.121 strain, which corresponds to the maximum shear stress. With a minor 0.015 increase of strain, the bond lengths of Al_{II}—O_{III}(long) drastically increase to 2.568 Å, signaling bond breaking and irreversible plastic deformation of the crystal. Compared with the bond stretching of Ga_{II}—O_{III}(long) bonds in β-Ga_2O_3 from 2.084 to 2.302 Å, the lengthening of Al_{II}—O_{III}(long) bonds during pure shear deformation is slightly smaller, but the stronger Al-O bonds induce much stronger stress over Ga-O bonds, preventing the crystal from plastic deformation. It is worth mentioning that the Al = 12.5 at. % and Al = 25 at. % structures exhibit a plateau after the ideal shear point, which can be attributed to the earlier breaking of Ga_{II}—O_{III} bonds relative to Al_{II}—O_{III} bonds. The growth intervals of both stress and strain rise with increasing Al concentration, i.e., the marginal benefit of Al alloying on ideal shear grows with Al alloying.

To gain further insights into the Al alloying effect on the mechanical properties of β-Ga_2O_3, the shear-stress-strain curves of β-$(Al_xGa_{1-x})_2O_3$ alloy along (100)/⟨010⟩, the second most plausible slip system, are also investigated and displayed in Fig. 9(b). Obvious increases for both ideal shear stress and ideal shear strain could be observed, with the ideal shear strain increasing from 0.148 (Al = 0 at. %) to 0.175 (Al = 50 at. %), i.e., by 18%, and the ideal shear stress increasing from 13.00 GPa (Al = 0 at. %) to 17.65 GPa (Al = 50 at. %), i.e., by 35.8%. The irreversible shear deformation of β-$(Al_xGa_{1-x})_2O_3$ alloy along the (100)/⟨010⟩ slip system could all be attributed to the significantly large shear component σ_4. Taken together with the ideal shear curves along the (001)/⟨010⟩ slip system, increases in both ideal shear stress-strain moduli could be observed, which further verifies the previous conclusion that, with increasing Al concentration, β-$(Al_xGa_{1-x})_2O_3$

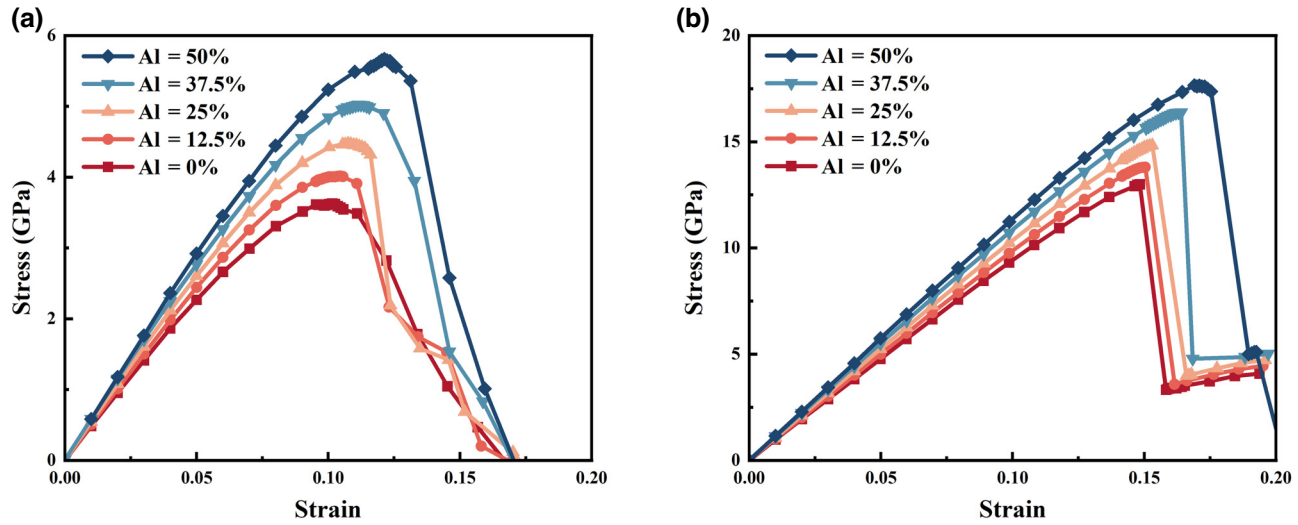

FIG. 9. (a) Ideal shear strengths of β-$(Al_xGa_{1-x})_2O_3$ ($0 \le x \le 0.5$) along the (001)/⟨010⟩ slip system; (b) ideal shear strengths of β-$(Al_xGa_{1-x})_2O_3$ ($0 \le x \le 0.5$) along the (100)/⟨010⟩ slip system.

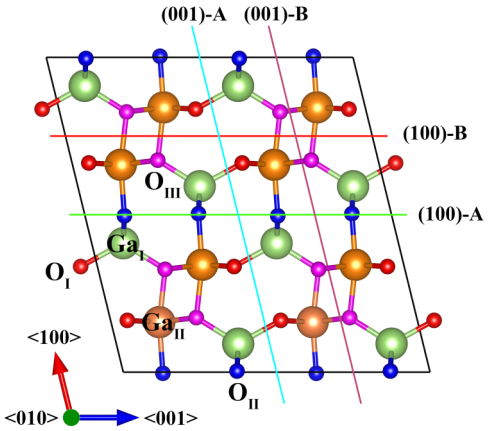

FIG. 10. Crystal structure of β-Ga_2O_3 projected along the ⟨010⟩-axis. (a) Two crystallographically inequivalent terminations of both (100) and (001) planes are labeled as "A" and "B", respectively.

alloy is more resistant to bond bending. In summary, the ideal shear strength of β-$(Al_xGa_{1-x})_2O_3$ alloy increases with increasing Al concentration.

D. Ideal cleavage strength

It has long been known that β-Ga_2O_3 possesses a primary cleavage plane (100) and a secondary cleavage plane (001) [23], which are detrimental to crystal growth, substrate processing, and device fabrication. There are two crystallographically inequivalent planes for both (100) and (001) cleavage planes due to the stacking nature of β-Ga_2O_3 [46], as shown in Fig. 10(a). The ideal cleavage strength is defined as the critical stress required to separate two neighboring crystallographic planes from each other. By means of first-principle calculations, the microscopic origin of the cleavage mechanism can be investigated [47]; the calculation methods are detailed in Appendix E.

Figure 11 shows the calculated energy difference and tensile stress along a certain cleavage orientation as a function of displacement for the four cleavage planes of β-Ga_2O_3. The ideal cleavage energies of (001)-A, (001)-B, (100)-A, and (100)-B are estimated to be 3.72, 2.48, 2.01, and 1.24 J/m^2, respectively, which is in good accordance with a previous study [48]. The ideal cleavage strengths of the (001)-A, (001)-B, (100)-A, and (100)-B planes are estimated to be 19.5, 18.4, 11.1, and 9.4 GPa, respectively. Among them, the (100)-B plane possesses the lowest cleavage energy and strength and the (001)-B plane is more favorable than the (001)-A plane. The origin of the higher cleavage energy and strength of (100)-A compared with (100)-B can be attributed to the stronger bonds of Ga_{II}—O_{II} relative to Ga_{II}—O_{III}(short), as these two planes possess the same bond density (i.e., 1.13×10^{19} m^{-2}). However, even though the Ga_{II}—O_{III}(long) bonds lying in the (001)-B planes are weaker than the Ga_{II}—O_{III}(short) bonds, the much higher bond density (2.14×10^{19} m^{-2}) compared with the (100) planes means that many more bond breaks are required for dissociation to occur and, thus, prevents it from cleavage. In general, the (001)-A plane is the strongest plane on account of the strongest Ga_I—O_{II} bonds.

The ideal cleavage energies and strengths of the (001) planes are overall higher than those of the (100) planes, which can explain why the (100)-plane is a more primary cleavage plane than the (001)-plane. It is worth mentioning that the ideal cleavage energy difference between the (100)-A and (100)-B planes is only 0.77 J/m^2, which may cause nonuniformity to (100) β-Ga_2O_3 substrates as these

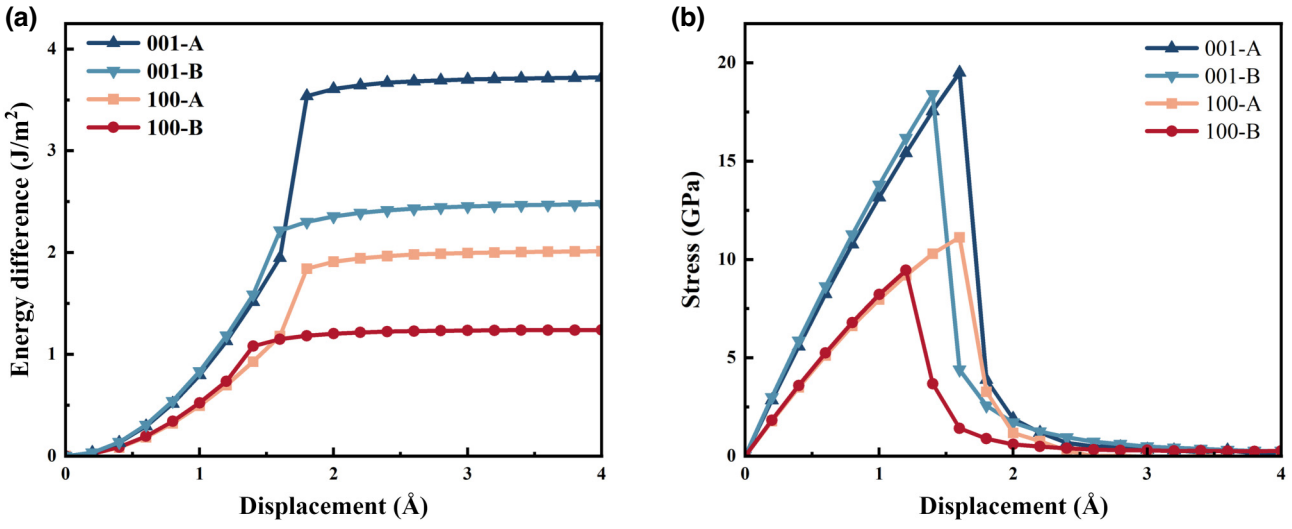

FIG. 11. Calculated (a) energy difference and (b) tensile stress component along the cleavage orientation of the (100)-A, (100)-B, (001)-A, and (001)-B planes versus displacement distance.

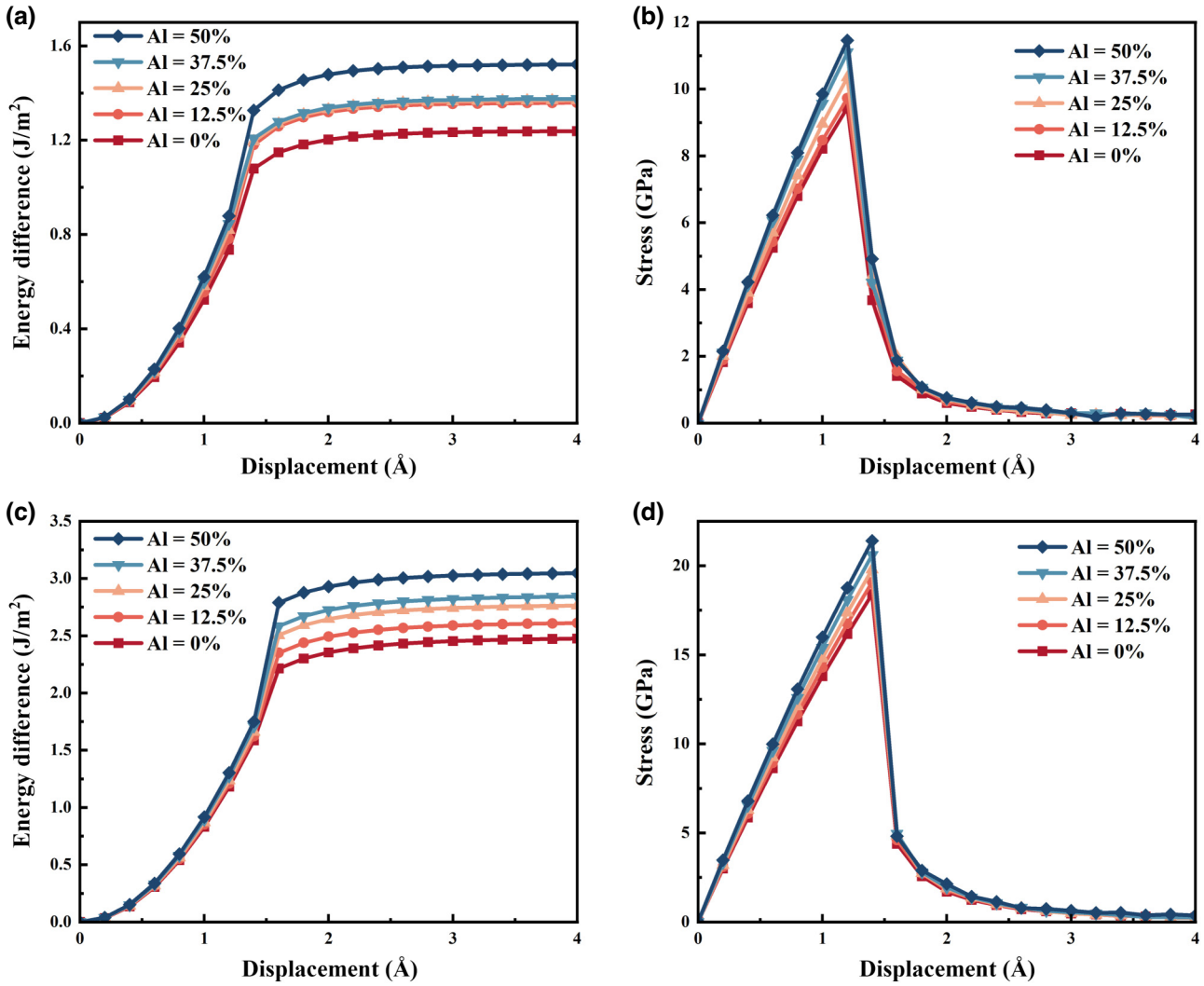

FIG. 12. Calculated (a) energy difference and (b) tensile stress component along the cleavage orientation of the (100)-B plane, (c) energy difference and (d) tensile stress component along the cleavage orientation of the (001)-B plane versus displacement distance.

two planes are competing at elevated temperatures [49], and further lead to the relativity poor epitaxy quality of GaN on (100) β-Ga_2O_3 substrates [50]. Taken together, the relativity weak Ga_{II}—O_{III}(short) bonds and low in-plane bond density are the main reasons for the low ideal cleavage energy of the (100)-B plane.

With Al alloying in the octahedral sites of β-Ga_2O_3, the ideal cleavage strengths and energies are enhanced. As shown in Figs. 12(a) and 12(b), by alloying with 50 at. % Al, the ideal cleavage energy of the (100)-B plane increases from 1.24 to 1.52 J/m^2, i.e., by 23%, and the ideal cleavage strength of the (100)-B plane increases from 9.4 to 11.5 GPa, i.e., by 22%. A similar enhancement is observed for the (001)-B planes, as shown in Figs. 12(c) and 12(d). The corresponding ideal cleavage energy increases from 2.48 to 3.05 J/m^2, i.e., by 23%, and the ideal cleavage strength increases from 18.4 to 21.4 GPa, i.e., by 16%. The overall enhancement of cleavage with increasing Al alloying concentration can also be observed, which can be attributed to the stronger Al_{II}—O_{III} bonds relative to the Ga_{II}—O_{III} bonds.

III. CONCLUSIONS

In summary, the effect of Al alloying on the mechanical properties of β-Ga_2O_3 is investigated by first-principle calculations. The elastic strengths, minimum ideal shear strength, and minimum cleavage strength are significantly enhanced with increasing Al concentration.

Microscopically, Al alloying introduces bond stiffening to the octahedral sites and bond rotation to the tetrahedral sites. The lattice contractions decrease the lattice mismatch between β-$(Al_xGa_{1-x})_2O_3$ and GaN from 2.8% at $x = 0$ to 1.1% at $x = 0.5$. The minimum Young's modulus and shear modulus increase by 20% with 50 at. % Al alloying. Pugh's ratio and Cauchy pressure analyses indicate that Al

alloyed β-Ga_2O_3 are less prone to ductile failure and more resistant to bond bending. In terms of ideal shear strength, the increase from 3.63 to 5.67 GPa (i.e., by 56.2%) along the most plausible activated (001)/⟨010⟩ slip system with 50 at. % Al alloying stems from bond stiffening. Ideal cleavage analysis determines the (100)-B plane to be the primary cleavage plane, which can be attributed to the weak Ga_{II}—O_{III}(short) bonds and the low in-plane bond density. With 50 at. % Al alloying, the 22% increase of the ideal cleavage strength of the (100)-B plane and the 16% increase of ideal cleavage strength of the (001)-B plane can effectively prevent the crystal from cleavage. Our calculations indicate that β-$(Al_xGa_{1-x})_2O_3$ alloys are favorable in terms of mechanical properties and can be utilized as seed crystals for β-Ga_2O_3 molten growth and substrates for GaN epitaxy.

The data that support the findings of this study are available from the corresponding author upon reasonable request.

ACKNOWLEDGMENTS

This work was supported by the "Pioneer" and "Leading Goose" R&D Program of Zhejiang (2023C01193), the National Natural Science Foundation of China (52202150, 22205203, and 62204218), Fundamental Research Funds for the Central Universities (226-2022-00200 and 226-2022-00250), the Foundation for Innovative Research Groups of the National Natural Science Foundation of China (61721005), the National Postdoctoral Program for Innovative Talents (BX20220264), the National Program for Support of Topnotch Young Professionals, Leading Innovative and Entrepreneur Team Introduction Program of Hangzhou (TD2022012), and the Open Fund of the State Key Laboratory of Optoelectronic Materials and Technologies (Sun Yat-sen University).

Y.Y.: formal analysis (lead); methodology (lead); data curation (lead); visualization (lead); writing (lead). C.L.: methodology (supporting); data curation (supporting). D.Y.: supervision (lead). H.Z.: resources (lead); supervision (lead). T.D.: conceptualization (lead); resources (lead); supervision (lead); writing – review and editing (lead).

The authors have no conflicts of interest to disclose.

APPENDIX A: FIRST-PRINCIPLE CALCULATIONS

The $1 \times 4 \times 2$ supercell models of β-$(Al_xGa_{1-x})_2O_3$ consisting of 160 atoms were utilized to construct quasicubic models for elastic constants and ideal shear strength calculations with three similar basis lattice vectors. The Al

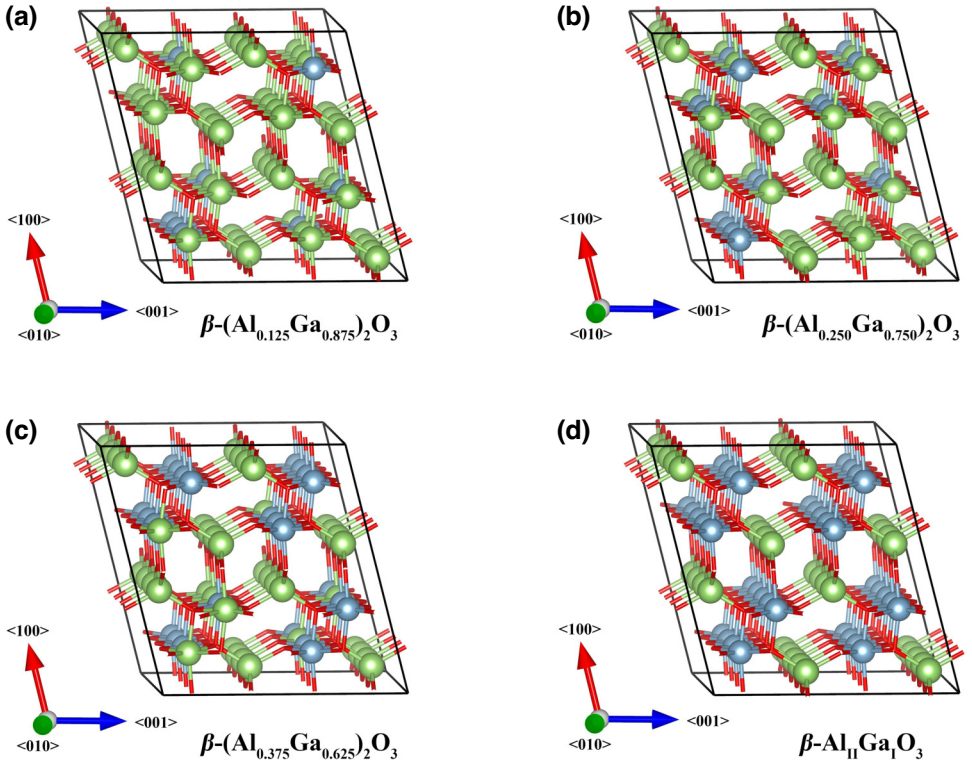

FIG. 13. Special quasirandom supercell structures of (a) β-$(Al_{0.125}Ga_{0.875})_2O_3$, (b) β-$(Al_{0.25}Ga_{0.75})_2O_3$, (c) β-$(Al_{0.375}Ga_{0.625})_2O_3$, and (d) β-$Al_{II}Ga_IO_3$. To emphasize the special distribution of Al atoms here, the inequivalent gallium and oxygen atoms are not labeled separately, and the oxygen atoms are hidden. The Al atoms are labeled in blue and the Ga atoms are labeled in green.

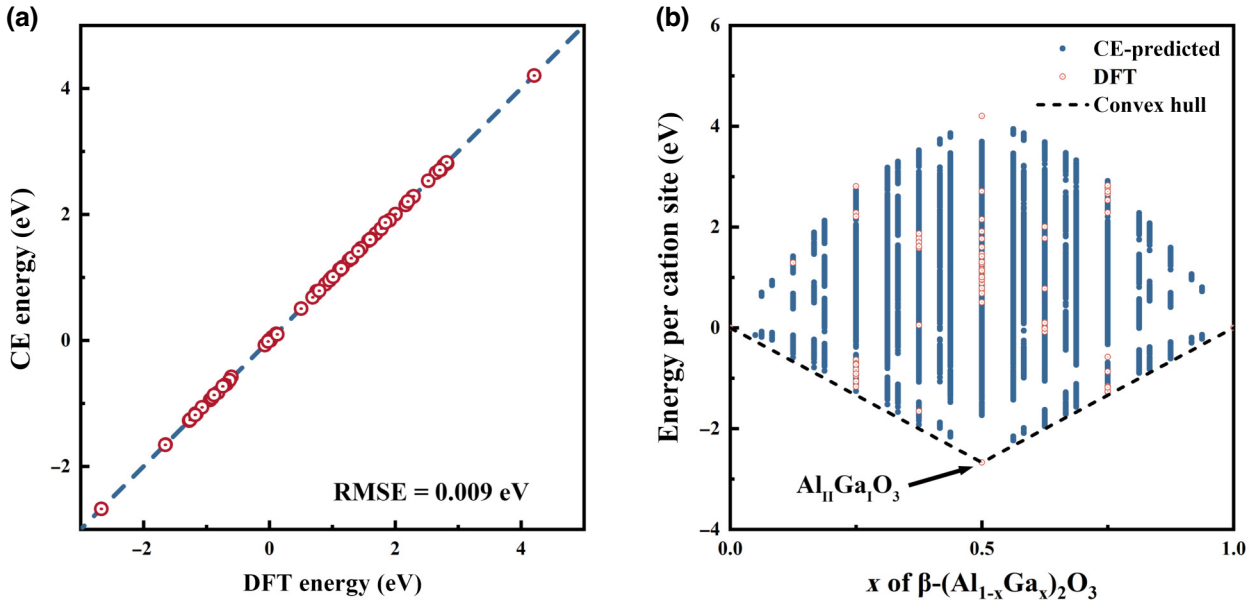

FIG. 14. Cluster expansion (CE) model. (a) Comparison between the energies per $(Al_xGa_{1-x})_2O_3$ formula predicted by the DFT calculations and CE model. (b) Energies of β-$(Al_xGa_{1-x})_2O_3$ alloys with different composition x and atomic configurations. The Al-ordered alloys with $0.0 < x < 0.5$ lie above the energy convex hull between β-Ga_2O_3 and the most stable ordered β-$Al_{II}Ga_IO_3$ alloy, whose Ga_{II} sites are completely substituted by Al.

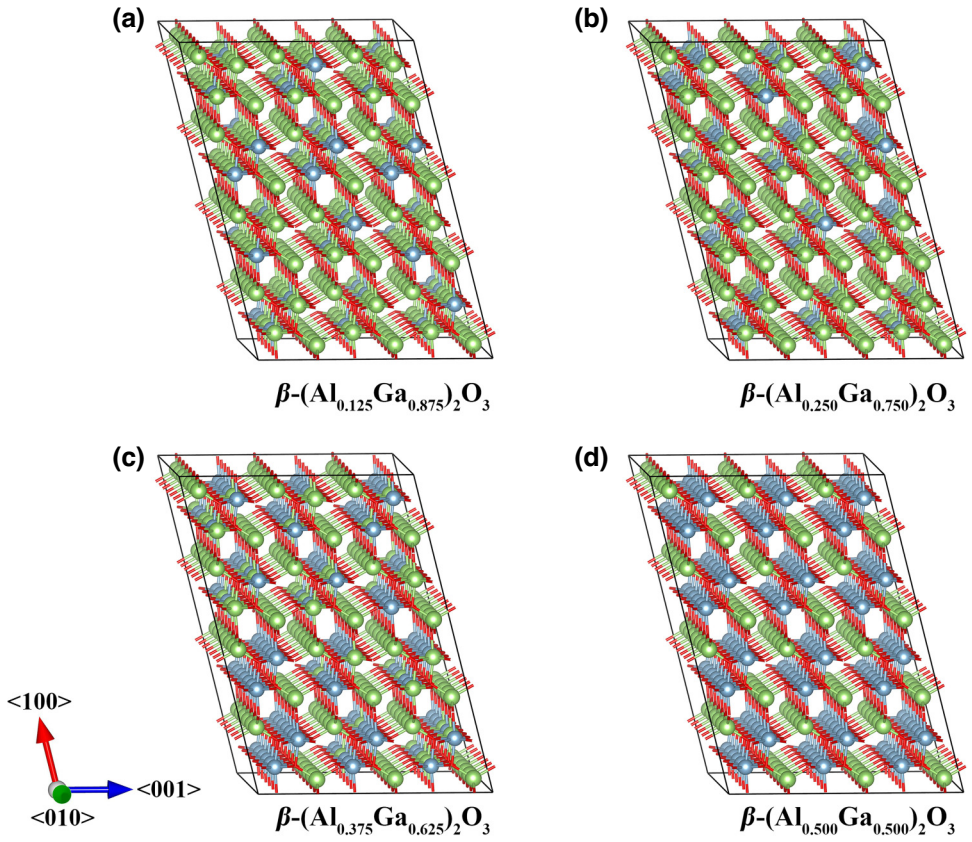

FIG. 15. Equilibrated structures from the Monte Carlo simulation of (a) β-$(Al_{0.125}Ga_{0.875})_2O_3$, (b) β-$(Al_{0.25}Ga_{0.75})_2O_3$, (c) β-$(Al_{0.375}Ga_{0.625})_2O_3$, and (d) β-$(Al_{0.500}Ga_{0.500})_2O_3$. No Al substitution on the Ga_I site is observed in any of these structures. To emphasize the special distribution of the Al atoms here, the inequivalent gallium and oxygen atoms are not labeled separately, and the oxygen atoms are hidden. The Al atoms are labeled in blue and the Ga atoms are labeled in green.

atoms preferably substitute the octahedral sites of β-Ga_2O_3 instead of the tetrahedral sites, as discussed in Appendix B. Thus, the 32 octahedral sites of β-Ga_2O_3 supercell are quasirandomly replaced by 8, 16, and 24 Al atoms and orderly replaced by 32 Al atoms. The schematic illustrations of the alloyed supercells are displayed in Fig. 13. For ideal cleavage strength calculations, the $2 \times 1 \times 1$ and $1 \times 1 \times 2$ supercells of the SQS models consisting of 320 atoms were utilized in order to prevent interactions between two cleavage planes in cleaving direction. All structures were visualized using VESTA [51].

All the DFT calculations are performed using the projected augmented wave method implemented in the VIENNA AB-INITIO SIMULATION PACKAGE (VASP) code [52]. The plane-wave basis cutoff is set to 900 eV. The structure optimizations are performed until all the residual stresses are smaller than 0.01 GPa. For solid materials, local density approximation often slightly underestimates the equilibrium lattice constants by about 1%, while the Perdew-Burke-Ernzerhof (PBE) functional usually overestimates them [53]. The revised PBE for solids (PBEsol) functional usually performs effectively for structure, energetic, mechanical, and vibrational properties in solids and is, thus, employed for the β-$(Al_xGa_{1-x})_2O_3$ alloy system.

APPENDIX B: VALIDATION OF Al SUBSTITUTION

To investigate the ordering of Al and Ga atoms in β-$(Al_xGa_{1-x})_2O_3$ alloy, we first construct the cluster expansion (CE) model describing the relation between alloy energy and atomic configuration. The CE coefficients are extracted from the DFT energies of periodic structure calculations with different Al and Ga occupations, as implemented in ATAT [54]. The 76 DFT calculations up to 20 atoms were performed and the resulting CE model exhibits a very small root mean squared error against the DFT data of 9 meV per $(Al_xGa_{1-x})_2O_3$ formula, demonstrating the excellent performance of the CE model.

In the CE model construction, Al substitutions on both Ga_I and Ga_{II} sites are included for model completeness. However, Al_{II} is energetically favored over Al_I, as demonstrated by both the energy convex hull and Monte Carlo simulations. As shown in Fig. 14(b), all ordered alloys with $0.0 < x < 0.5$ lie above the energy convex hull between β-Ga_2O_3 and the most stable ordered β-$Al_{II}Ga_IO_3$ alloy whose Ga_{II} sites are completely substituted by Al. Moreover, there are many configurations

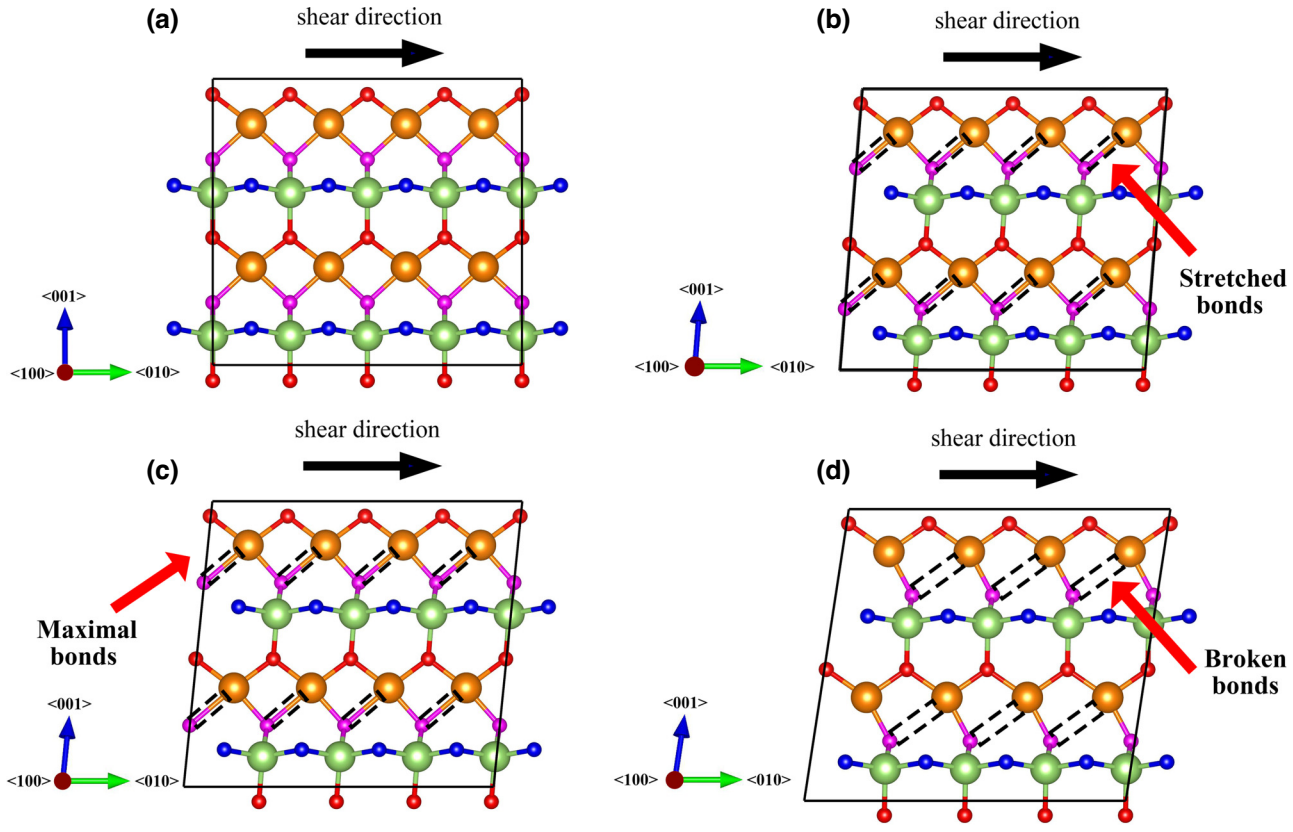

FIG. 16. Crystal structures projected along the ⟨100⟩-axis of β-Ga_2O_3 sheared along the (001)/⟨010⟩ slip system: (a) unsheared structure at shear strain = 0.000; (b) sheared structure at strain = 0.080 with stretched Ga_{II}—O_{III}(long) bonds; (c) sheared structure before the critical bond breaking point at strain = 0.102; (d) sheared structure with broken Ga_{II}—O_{III}(long) bonds at strain = 0.150.

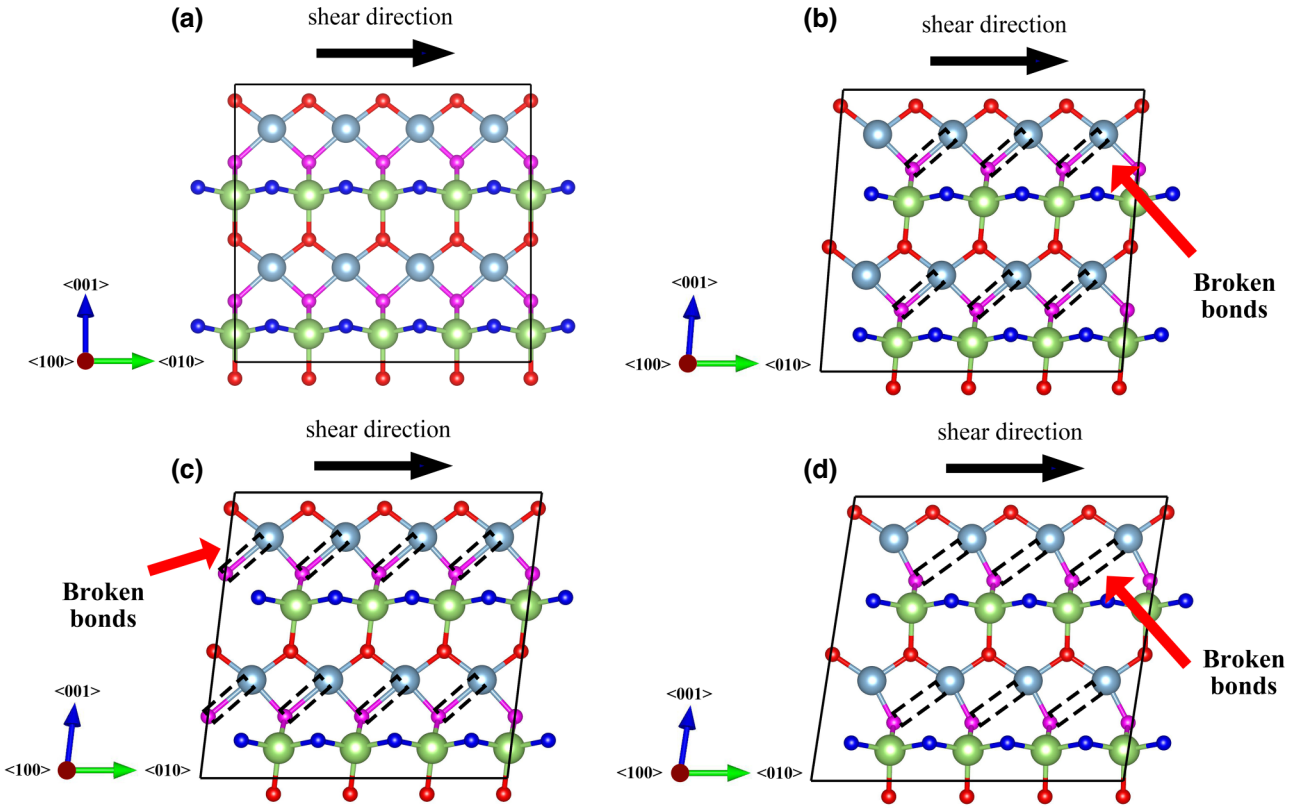

FIG. 17. Crystal structures projected along the ⟨100⟩-axis of β-$Al_{II}Ga_IO_3$ sheared along the (001)/⟨010⟩ slip system: (a) unsheared structure at shear strain = 0.000; (b) sheared structure at strain = 0.080 with stretched Ga_{II}—O_{III}(long) bonds; (c) sheared structure before the critical bond breaking point at strain = 0.121; (d) sheared structure with broken Ga_{II}—O_{III}(long) bonds at strain = 0.150.

that are only slightly above the convex hull. This means that at finite temperature, the β-$(Al_xGa_{1-x})_2O_3$ alloys with $0.0 < x < 0.5$ are likely random alloys between β-Ga_2O_3 and β-$Al_{II}Ga_IO_3$. In such alloys, Ga_I sites remain unsubstituted while the Ga_{II} sites are randomly Al-substituted.

To confirm such an assumption, we performed Monte Carlo simulations on the canonical ensemble at 300 K. A supercell consisting of 720 atoms was employed, and simulations were performed for $x = 0.125$, 0.250, 0.375, and 0.500. As shown in the equilibrated structures in Fig. 15, none of the Ga_I sites was substituted by Al, confirming the energetic preference of Al_{II} over Al_I. In addition, the Ga_{II} sites are randomly substituted by Al. Therefore, in the spirit of special quasirandom structure, we study the mechanical properties of β-$(Al_xGa_{1-x})_2O_3$ alloys with SQS cells with randomly occupied Al_{II} sites.

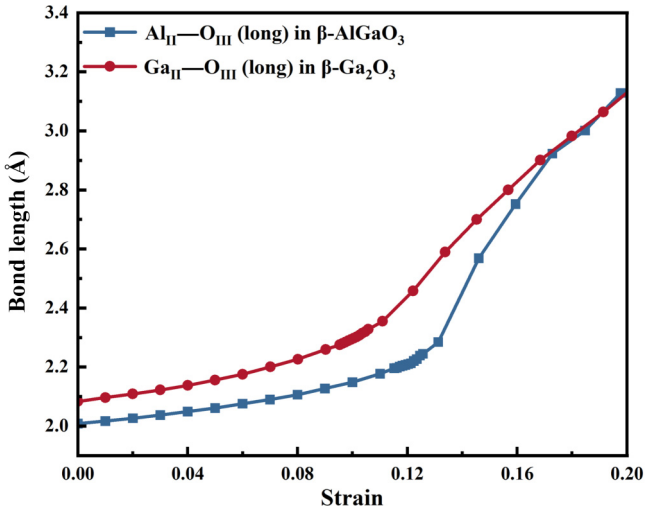

FIG. 18. Bond length variation curves of Ga_{II}—O_{III}(long) in β-Ga_2O_3 and Al_{II}—O_{III}(long) in β-$Al_{II}Ga_IO_3$ during pure shear deformation along the (001)/⟨010⟩ slip plane. The critical breakdown strains of Ga_{II}—O_{III}(long) and Al_{II}—O_{III}(long) bonds are determined to be 0.102 and 0.121, respectively. The critical breakdown bond lengths of Ga_{II}—O_{III}(long) and Al_{II}—OI_{II}(long) bonds are determined to be 2.30 and 2.21 Å, respectively.

APPENDIX C: INTERATOMIC FORCE CONSTANTS AND ELASTIC CONSTANTS

To analyze the bond-stiffening effect introduced by Al alloying, the traces of IFC tensors are calculated. The IFC tensor Φ_{kl} from first-principle calculations is given by the

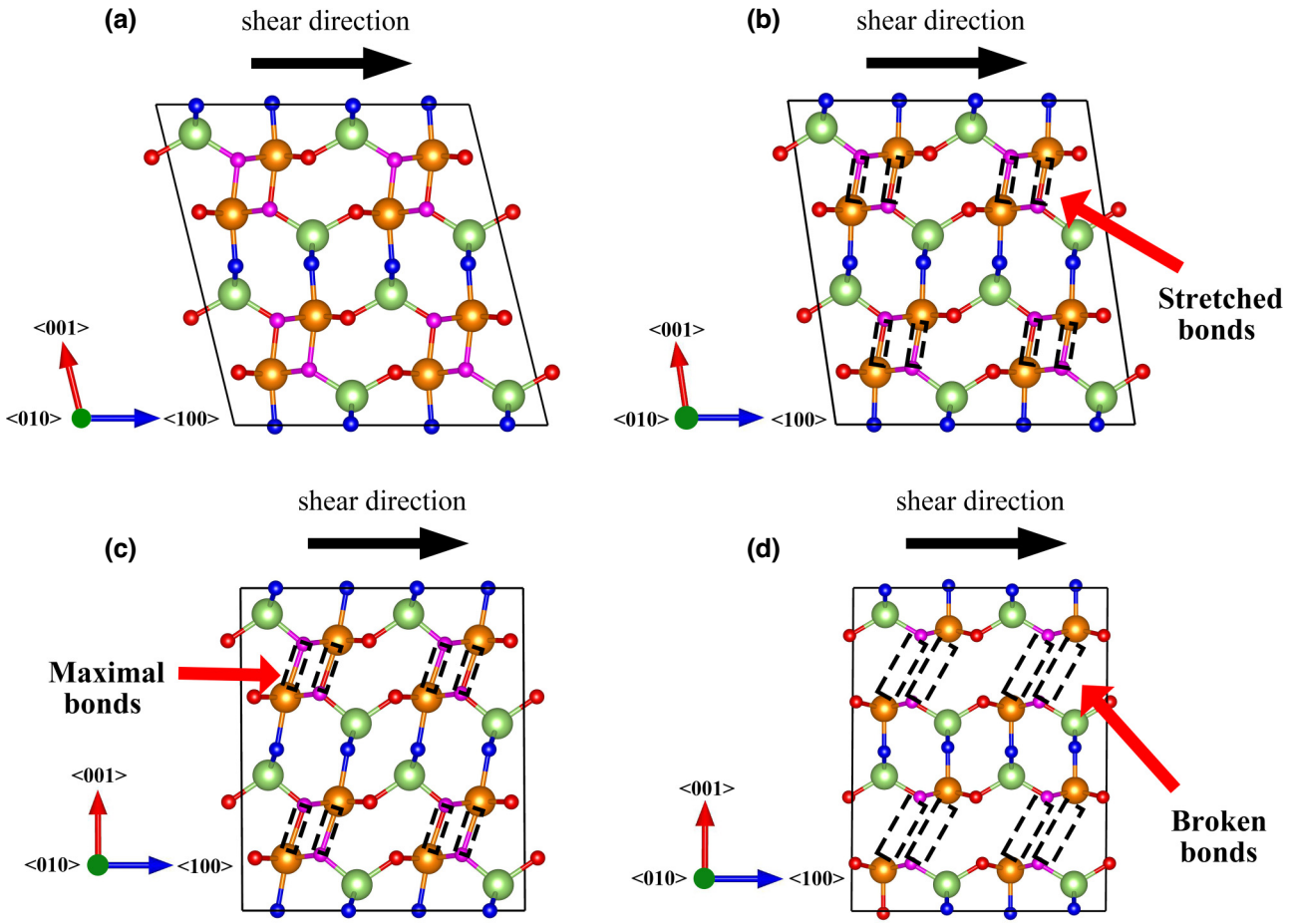

FIG. 19. Crystal structures projected along the ⟨010⟩-axis of β-Ga_2O_3 sheared along the (001)/⟨100⟩ slip system: (a) unsheared structure at shear strain = 0.000; (b) sheared structure at strain = 0.080 with stretched Ga_{II}—O_{III}(short) bonds; (c) sheared structure before the critical bond breaking point at strain = 0.262; (d) sheared structure with broken Ga_{II}—O_{III}(short) bonds at strain = 0.300.

following:

$$\Phi_{kl} = \begin{bmatrix} \frac{\partial^2 E}{\partial u_{Ix}\partial u_{Ix}} & \frac{\partial^2 E}{\partial u_{Ix}\partial u_{Iy}} & \frac{\partial^2 E}{\partial u_{Ix}\partial u_{Iz}} \\ \frac{\partial^2 E}{\partial u_{Iy}\partial u_{Ix}} & \frac{\partial^2 E}{\partial u_{Iy}\partial u_{Iy}} & \frac{\partial^2 E}{\partial u_{Iy}\partial u_{Iz}} \\ \frac{\partial^2 E}{\partial u_{Iz}\partial u_{Ix}} & \frac{\partial^2 E}{\partial u_{Iz}\partial u_{Iy}} & \frac{\partial^2 E}{\partial u_{Iz}\partial u_{Iz}} \end{bmatrix}, \tag{C1}$$

where E and $u_{I\alpha}$ represent the total energy and α-direction (i.e., x, y, or z) component of the atoms and atomic displacement of I, respectively. The trace of this tensor stands for an explicit criterion toward bonding stiffness, regardless of crystal structure or coordinate system.

To investigate the mechanical properties, elastic constants C_{ij} calculations are performed utilizing the stress-strain relationship implemented in *VASPKIT* [55]. The stress tensor σ and strain tensor ε can be denoted as follows:

$$\sigma = \begin{bmatrix} \sigma_{11} & \sigma_{12} & \sigma_{13} \\ \sigma_{21} & \sigma_{22} & \sigma_{23} \\ \sigma_{31} & \sigma_{32} & \sigma_{33} \end{bmatrix}, \tag{C2}$$

$$\varepsilon = \begin{bmatrix} \varepsilon_{11} & \varepsilon_{12} & \varepsilon_{13} \\ \varepsilon_{21} & \varepsilon_{22} & \varepsilon_{23} \\ \varepsilon_{31} & \varepsilon_{32} & \varepsilon_{33} \end{bmatrix}, \tag{C3}$$

both of which are symmetric matrices with three diagonal normal components and three independent shear components. Simplifying via Voigt notation, the stress-strain tensor can be related through the elastic constants C_{ij}, i.e.,

$$\sigma_i = \sum_{j=1}^{6} C_{ij}\varepsilon_j, \tag{C4}$$

where there are six independent components for both stress tensor σ_i and strain tensor ε_j, i.e., $1 \le i, j \le 6$. In addition, the elastic constants are represented by a fourth-order tensor that is a 6×6 symmetric matrix in Voigt notation.

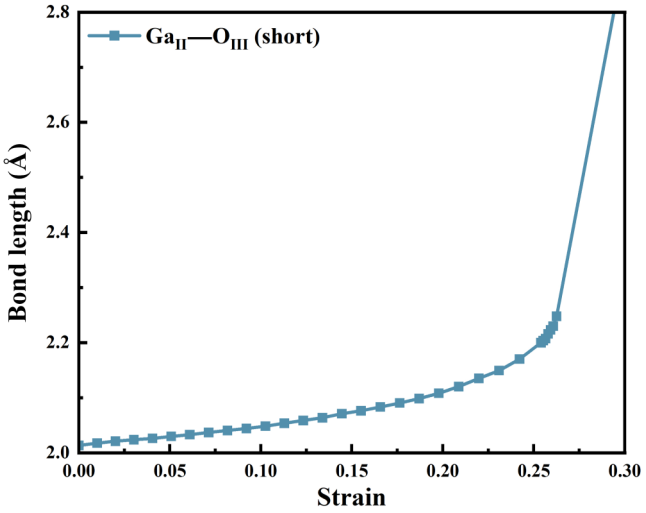

FIG. 20. Bond length variation curves of Ga_{II}—O_{III}(short) in β-Ga_2O_3 during pure shear deformation along the (001)/⟨100⟩ slip plane. The critical breakdown strain of the Ga_{II}—O_{III}(short) bonds is determined to be 0.262. The critical breakdown bond length of the Ga_{II}—O_{III}(short) bonds is found to be 2.25 Å.

By deforming the crystal with a series of distortions and calculating the corresponding σ and ε, the elastic constants can be derived.

APPENDIX D: IDEAL SHEAR STRENGTH

To obtain the ideal shear strength of β-$(Al_xGa_{1-x})_2O_3$ alloys, calculations were performed with pure affine shear deformations along different shear planes. The atom coordinates are unchanged during the initial affine shear deformations. Affine deformation of a certain lattice can be expressed with a second-order deformation tensor $\boldsymbol{F}$, which is denoted as:

$$\boldsymbol{D}_{\text{deform}} = \boldsymbol{D}_0\boldsymbol{F}, \tag{D1}$$

where $\boldsymbol{D}_0$ and $\boldsymbol{D}_{\text{deform}}$ are the lattice vectors before and after deformation, respectively. A simple shear deformation can, thus, be performed by $\boldsymbol{F}$, which can be expressed as:

$$\boldsymbol{F} = \begin{bmatrix} 1 & \varepsilon & 0 \\ 0 & 1 & 0 \\ 0 & 0 & 1 \end{bmatrix}, \tag{D2}$$

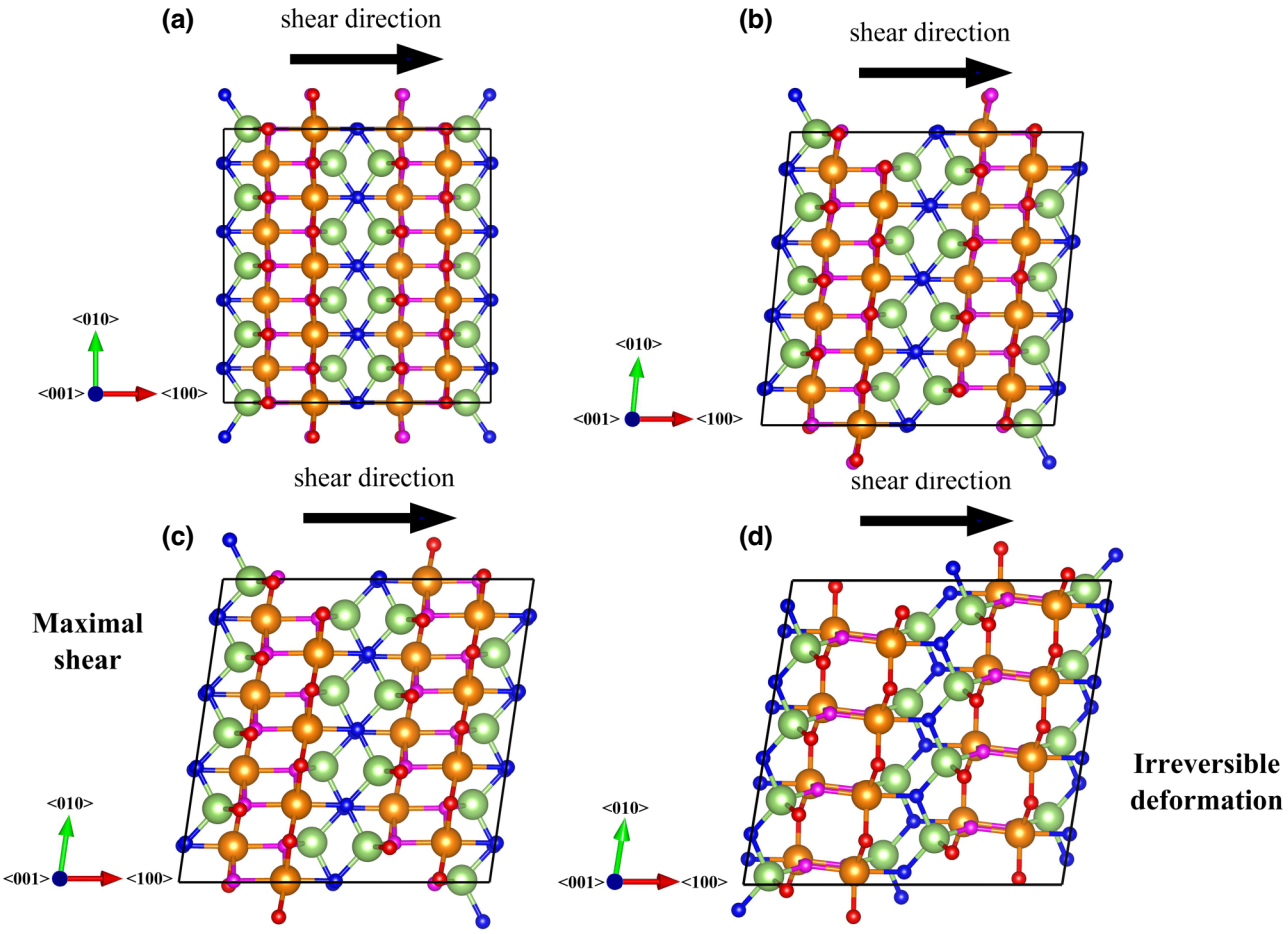

FIG. 21. Crystal structures projected along the ⟨001⟩-axis of β-Ga_2O_3 sheared along the (100)/⟨010⟩ slip system: (a) unsheared structure at shear strain = 0.000; (b) sheared structure at strain = 0.080; (c) sheared structure before the critical lattice deformation at strain = 0.148; (d) sheared structure with irreversible lattice deformation at strain = 0.160.

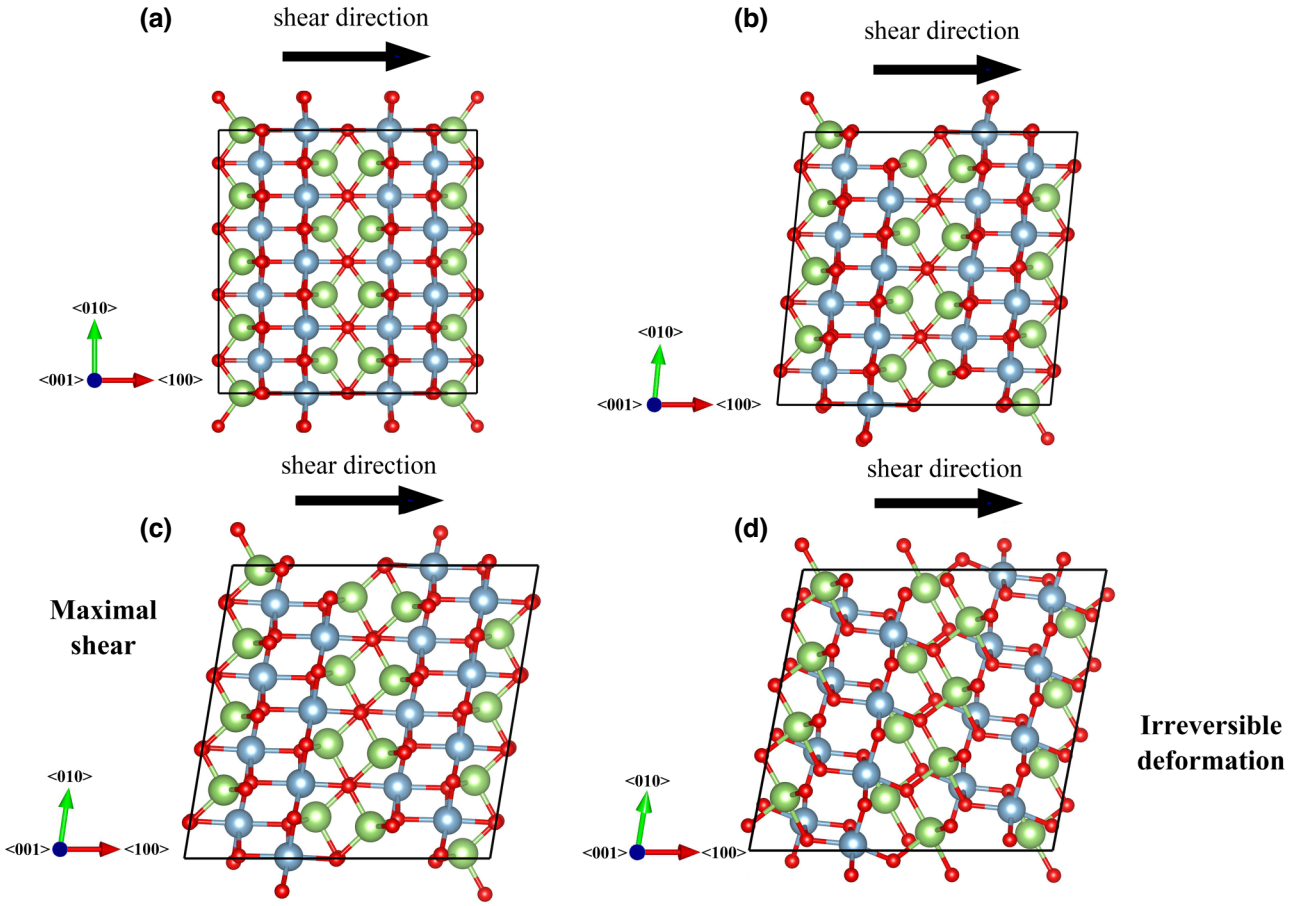

FIG. 22. Crystal structures projected along the ⟨001⟩-axis of β-$Al_{II}Ga_{I}O_3$ sheared along the (100)/⟨010⟩ slip system: (a) unsheared structure at shear strain = 0.000; (b) sheared structure at strain = 0.010; (c) sheared structure before the critical lattice deformation at strain = 0.175; (d) sheared structure with irreversible lattice deformation at strain = 0.180.

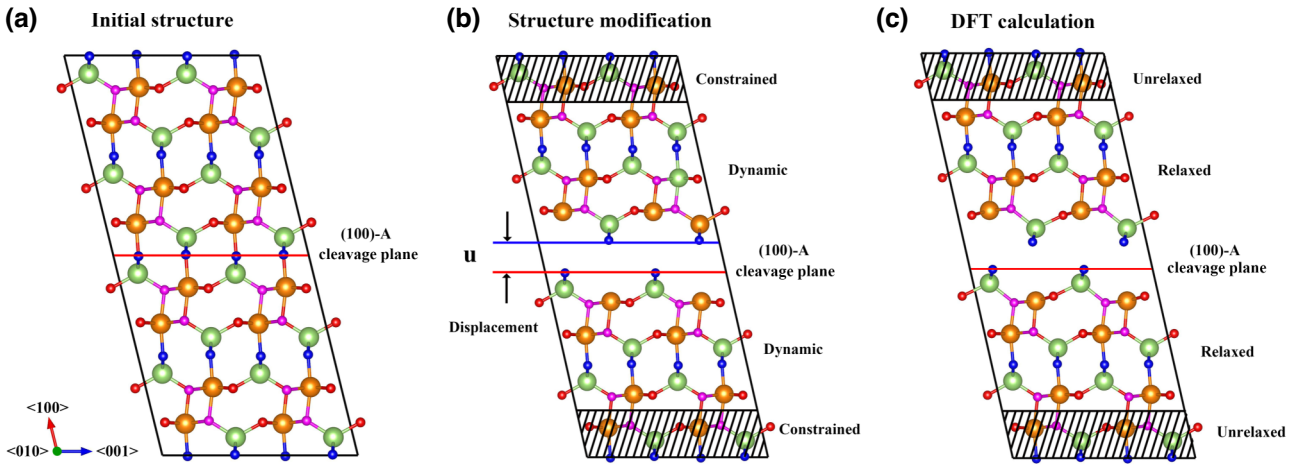

FIG. 23. (a) Initial structure of the doubled supercell along the ⟨100⟩-orientation with the (100)-A cleavage plane; (b) structure modification involving displacing the atoms above the cleavage plane along a certain direction with a separation displacement u; (c) cleavage structure undergoing structure relaxation.

where ε is the only shear component corresponding to the engineering shear strain.

After the initial deformation, the structures are fully relaxed with the constraint on the applied shear component, and the ideal shear strength can be derived as the maximum shear stress the unit cell can endure.

The structures projected along the ⟨100⟩-axis of β-Ga_2O_3 and β-$Al_{II}Ga_IO_3$ during pure shear deformation along the (001)/⟨010⟩ slip system are displayed in Figs. 16 and 17, respectively. The corresponding bond length variation curves of Ga_{II}—O_{III}(long) and Al_{II}—O_{III}(long) bonds are shown in Fig. 18. The structures projected along the ⟨010⟩-axis of β-Ga_2O_3 and the corresponding bond length variation curve of Ga_{II}—O_{III}(short) bonds during pure shear deformation along the (001)/⟨100⟩ slip system are displayed in Figs. 19 and 20, respectively. The structures projected along the ⟨001⟩-axis of β-Ga_2O_3 and β-$Al_{II}Ga_IO_3$ during pure shear deformation along the (100)/⟨010⟩ slip system are shown in Figs. 21 and 22, respectively.

APPENDIX E: IDEAL CLEAVAGE STRENGTH

To obtain the ideal cleavage strength of β-$(Al_xGa_{1-x})_2O_3$, alias deformations were performed by cleaving two neighboring crystallographic planes along a certain direction with a separation distance, u. Taking the cleavage process of the (100)-A plane as an example, the initial structure of the doubled supercell along the ⟨100⟩-orientation is displayed in Fig. 23(a). The modification of the initial structure involves cleaving two neighboring crystallographic planes along a certain direction with a separation displacement, u, as shown in Fig. 23(b). The coordinates of the three atom planes beside the cleavage plane (approximately 7.5 Å from the cleavage plane) are fully dynamic while the rest of the atoms and lattice are constrained. Finally, the modified structure is fully relaxed, as shown in Fig. 23(c). The ideal cleavage strength can, thus, be calculated as the maximal tensile stress component along the cleavage orientation.

[1] M. Higashiwaki, K. Sasaki, A. Kuramata, T. Masui, and S. Yamakoshi, Gallium oxide (Ga_2O_3) metal-semiconductor field-effect transistors on single-crystal β-Ga_2O_3 (010) substrates, Appl. Phys. Lett. **100**, 013504 (2012).

[2] S. Sharma, L. Meng, A. F. M. A. U. Bhuiyan, Z. Feng, D. Eason, H. Zhao, and U. Singisetti, Vacuum annealed β-Ga_2O_3 recess channel MOSFETs with 8.56 kV breakdown voltage, IEEE Electron Device Lett. **43**, 2029 (2022).

[3] H. Liu, Y. Wang, Y. Lv, S. Han, T. Han, S. Dun, H. Guo, A. Bu, and Z. Feng, 10-kV lateral β-Ga_2O_3 MESFETs with B ion implanted planar isolation, IEEE Electron Device Lett. **44**, 1048 (2023).

[4] Y. Lv, X. Zhou, S. Long, X. Song, Y. Wang, S. Liang, Z. He, T. Han, X. Tan, Z. Feng, *et al.*, Source-field-plated β-Ga_2O_3 MOSFET with record power figure of merit of 50.4 MW/cm^2, IEEE Electron Device Lett. **40**, 83 (2019).

[5] K. Tetzner, E. B. Treidel, O. Hilt, A. Popp, S. B. Anooz, G. Wagner, A. Thies, K. Ickert, H. Gargouri, and J. Würfl, Lateral 1.8 kV β-Ga_2O_3 MOSFET with 155 MW/cm^2 power figure of merit, IEEE Electron Device Lett. **40**, 1503 (2019).

[6] R. Togashi, K. Nomura, C. Eguchi, T. Fukizawa, K. Goto, Q. T. Thieu, H. Murakami, Y. Kumagai, A. Kuramata, S. Yamakoshi, *et al.*, Thermal stability of β-Ga_2O_3 in mixed flows of H_2 and N_2, Jpn. J. Appl. Phys. **54**, 041102 (2015).

[7] S. Ohira, N. Suzuki, N. Arai, M. Tanaka, T. Sugawara, K. Nakajima, and T. Shishido, Characterization of transparent and conducting Sn-doped β-Ga_2O_3 single crystal after annealing, Thin Solid Films **516**, 5763 (2008).

[8] Z. Jin, Y. Liu, N. Xia, X. Guo, Z. Hong, H. Zhang, and D. Yang, Wet etching in β-Ga_2O_3 bulk single crystals, CrystEngComm **24**, 1127 (2022).

[9] Z. Galazka, A. Fiedler, A. Popp, S. Ganschow, A. Kwasniewski, P. Seyidov, M. Pietsch, A. Dittmar, S. B. Anooz, K. Irmscher, *et al.*, Bulk single crystals and physical properties of β-$(Al_xGa_{1-x})_2O_3$ ($x = 0$–0.35) grown by the Czochralski method, J. Appl. Phys. **133**, 035702 (2023).

[10] Z. Galazka, K. Irmscher, R. Uecker, R. Bertram, M. Pietsch, A. Kwasniewski, M. Naumann, T. Schulz, R. Schewski, D. Klimm, *et al.*, On the bulk β-Ga_2O_3 single crystals grown by the Czochralski method, J. Cryst. Growth **404**, 184 (2014).

[11] A. Kuramata, K. Koshi, S. Watanabe, Y. Yamaoka, T. Masui, and S. Yamakoshi, High-quality β-Ga_2O_3 single crystals grown by edge-defined film-fed growth, Jpn. J. Appl. Phys. **55**, 1202A2 (2016).

[12] M. Higashiwaki, β-Ga_2O_3 material properties, growth technologies, and devices: A review, AAPPS Bull. **32**, 3 (2022).

[13] K. Hoshikawa, T. Kobayashi, E. Ohba, and T. Kobayashi, 50 mm diameter Sn-doped (001) β-Ga_2O_3 crystal growth using the vertical Bridgeman technique in ambient air, J. Cryst. Growth **546**, 125778 (2020).

[14] N. Xia, Y. Liu, D. Wu, L. Li, K. Ma, J. Wang, H. Zhang, and D. Yang, β-Ga_2O_3 bulk single crystals grown by a casting method, J. Alloys Compd. **935**, 168036 (2023).

[15] A. Nawaz, W. G. Mao, C. Lu, and Y. G. Shen, Nano-scale elastic-plastic properties and indentation-induced deformation of single crystal 4H-SiC, J. Mech. Behav. Biomed. Mater. **66**, 172 (2017).

[16] P. Kavouras, I. Ratschinski, G. P. Dimitrakopulos, H. S. Leipner, P. Komninou, G. Leibiger, and F. Habel, Deformation and fracture in (0001) and (10–10) GaN single crystals, Mater. Sci. Technol. **34**, 1531 (2018).

[17] Z. Guo, A. Verma, X. Wu, F. Sun, A. Hickman, T. Masui, A. Kuramata, M. Higashiwaki, D. Jena, and T. Luo, Anisotropic thermal conductivity in single crystal β-gallium oxide, Appl. Phys. Lett. **106**, 111909 (2015).

[18] K. Adachi, H. Ogi, N. Takeuchi, N. Nakamura, H. Watanabe, T. Ito, and Y. Ozaki, Unusual elasticity of monoclinic $\beta-Ga_2O_3$, J. Appl. Phys. **124**, 085102 (2018).

[19] S. Luan, L. Dong, and R. Jia, Analysis of the structural, anisotropic elastic and electronic properties of β-Ga_2O_3 with various pressures, J. Cryst. Growth **505**, 74 (2019).

[20] K. Lion, P. Pavone, and C. Draxl, Elastic stability of Ga_2O_3: Addressing the β to α phase transition from first principles, Phys. Rev. Mater. **6**, 013601 (2022).

[21] C. Zhang, X. Wu, Y. Xing, L. Zhou, H. Zhou, S. Li, and N. Xu, A first-principles study of hydrostatic strain engineering on the electronic properties of β-Ga_2O_3, Phys. B **660**, 414851 (2023).

[22] S. Gao, X. Yang, J. Cheng, X. Guo, and R. Kang, Deformation and fracture behaviors of monocrystalline β-Ga_2O_3 characterized using indentation method and first-principles calculations, Mater. Charact. **200**, 112920 (2023).

[23] T. Hou, W. Zhang, W. Mu, C. Li, X. Li, X. Ma, J. Zhang, H. Wang, Z. Jia, D. Liu, *et al.*, The anisotropy dependence of deformation mechanism of cleavage planes in β-Ga_2O_3 single crystal, Mater. Sci. Semicond. Process. **158**, 107357 (2023).

[24] J. Zhang, J. Shi, D.-C. Qi, L. Chen, and K. H. L. Zhang, Recent progress on the electronic structure, defect, and doping properties of Ga_2O_3, APL Mater. **8**, 020906 (2020).

[25] M. Mizuno, T. Yamada, and T. Noguchi, The liquidus curve in the system Al_2O_3-Ga_2O_3 as measured with a solar furnace, J. Ceram. Assoc. Jpn. **83**, 175 (1975).

[26] H. Peelaers, J. B. Varley, J. S. Speck, and C. G. Van de Walle, Structural and electronic properties of Ga_2O_3-Al_2O_3 alloys, Appl. Phys. Lett. **112**, 242101 (2018).

[27] N. K. Kalarickal, Z. Xia, J. F. McGlone, Y. Liu, W. Moore, A. R. Arehart, S. A. Ringel, and S. Rajan, High electron density β-$(Al_{0.17}Ga_{0.83})_2O_3/Ga_2O_3$ modulation doping using an ultra-thin (1 nm) spacer layer, J. Appl. Phys. **127**, 215706 (2020).

[28] A. F. M. A. U. Bhuiyan, Z. Feng, J. M. Johnson, H.-L. Huang, J. Hwang, and H. Zhao, MOCVD growth of β-phase $(Al_xGa_{1-x})_2O_3$ on (-201) β-Ga_2O_3 substrates, Appl. Phys. Lett. **117**, 142107 (2020).

[29] R. Wakabayashi, T. Oshima, M. Hattori, K. Sasaki, T. Masui, A. Kuramata, S. Yamakoshi, K. Yoshimatsu, and A. Ohtomo, Oxygen-radical-assisted pulsed-laser deposition of β-Ga_2O_3 and β-$(Al_xGa_{1-x})_2O_3$ films, J. Cryst. Growth **424**, 77 (2015).

[30] T. Deng, D. Yang, and X. Pi, Phonon-limited carrier mobilities and Hall factors in 4H-SiC from first principles, Phys. Rev. B **107**, 235203 (2023).

[31] J. Schmidt, H.-C. Wang, T. F. T. Cerqueira, S. Botti, and M. A. L. Marques, A dataset of 175 k stable and metastable materials calculated with the PBEsol and SCAN functionals, Sci. Data **9**, 64 (2022).

[32] S. Geller, Crystal structure of β-Ga_2O_3, J. Chem. Phys. **33**, 676 (1960).

[33] A. F. M. A. U. Bhuiyan, Z. Feng, H.-L. Huang, L. Meng, J. Hwang, and H. Zhao, Band offsets at metalorganic chemical vapor deposited β-$(Al_xGa_{1-x})_2O_3/\beta$-$Ga_2O_3$ interfaces—Crystalline orientation dependence, J. Vac. Sci. Technol., A **39**, 063207 (2021).

[34] E. G. Víllora, K. Shimamura, K. Kitamura, K. Aoki, and T. Ujiie, Epitaxial relationship between wurtzite GaN and β-Ga_2O_3, Appl. Phys. Lett. **90**, 234102 (2007).

[35] R. R. Reeber and K. Wang, Lattice parameters and thermal expansion of GaN, J. Mater. Res. **15**, 40 (2000).

[36] M. Leszczynski, T. Suski, P. Perlin, H. Teisseyre, I. Grzegory, M. Bockowski, J. Jun, S. Porowski, and J. Major, Lattice constants, thermal expansion and compressibility of gallium nitride, J. Phys. D: Appl. Phys. **28**, A149 (1995).

[37] R. Karpagam, S. L. S. Vimalraj, G. K. Sathishkumar, V. Megala, Y. Gowthami, and B. Balaji, DC and RF performance analysis of extended field plated AlGaN/GaN/β-Ga_2O_3 HEMT, Trans. Electr. Electron. Mater. **24**, 459 (2023).

[38] J. Furthmüller and F. Bechstedt, Quasiparticle bands and spectra of Ga_2O_3 polymorphs, Phys. Rev. B **93**, 115204 (2016).

[39] R. Hill, The elastic behaviour of a crystalline aggregate, Proc. Phys. Soc., London, Sect. A **65**, 349 (1952).

[40] R. P. Thompson and W. J. Clegg, Predicting whether a material is ductile or brittle, Curr. Opin. Solid State Mater. Sci. **22**, 100 (2018).

[41] S. Ogata, J. Li, and S. Yip, Ideal pure shear strength of aluminum and copper, Science **298**, 807 (2002).

[42] S. Xu, W.-R. Jian, and I. J. Beyerlein, Ideal simple shear strengths of two HfNbTaTi-based quinary refractory multi-principal element alloys, APL Mater. **10**, 111107 (2022).

[43] G. Li, U. Aydemir, S. I. Morozov, S. A. Miller, Q. An, W. A. Goddard, P. Zhai, Q. Zhang, and G. J. Snyder, Mechanical properties in thermoelectric oxides: Ideal strength, deformation mechanism, and fracture toughness, Acta Mater. **149**, 341 (2018).

[44] L. Casillas-Trujillo, L. Xu, and H. Xu, Compositional effects on ideal shear strength in Fe-Cr alloys, J. Alloys Compd. **720**, 466 (2017).

[45] Q. An and G. Li, Shear-induced mechanical failure of β-Ga_2O_3 from quantum mechanics simulations, Phys. Rev. B **96**, 144113 (2017).

[46] V. M. Bermudez, The structure of low-index surfaces of β-Ga_2O_3, Chem. Phys. **323**, 193 (2006).

[47] S. H. Zhang, Z. H. Fu, and R. F. Zhang, ADAIS: Automatic derivation of anisotropic ideal strength via high-throughput first-principles computations, Comput. Phys. Commun. **238**, 244 (2019).

[48] J. Sun and J. Leng, Tuning the electronic structure of quasi-two-dimensional β-Ga_2O_3 by vacancy and doping, Phys. B **552**, 195 (2019).

[49] T. C. Lovejoy, E. N. Yitamben, N. Shamir, J. Morales, E. G. Villora, K. Shimamura, S. Zheng, F. S. Ohuchi, and M. A. Olmstead, Surface morphology and electronic structure of bulk single crystal β-Ga_2O_3(100), Appl. Phys. Lett. **94**, 081906 (2009).

[50] M. M. Muhammed, M. A. Roldan, Y. Yamashita, S. L. Sahonta, I. A. Ajia, K. Iizuka, A. Kuramata, C. J. Humphreys, and I. S. Roqan, High-quality III-nitride films on conductive, transparent (-201)-oriented β-Ga_2O_3 using a GaN buffer layer, Sci. Rep. **6**, 29747 (2016).

[51] K. Momma and F. Izumi, VESTA 3 for three-dimensional visualization of crystal, volumetric and morphology data, J. Appl. Crystallogr. **44**, 1272 (2011).

[52] G. Kresse and J. Furthmüller, Efficient iterative schemes for ab initio total-energy calculations using a plane-wave basis set, Phys. Rev. B **54**, 11169 (1996).

[53] J. P. Perdew, A. Ruzsinszky, G. I. Csonka, O. A. Vydrov, G. E. Scuseria, L. A. Constantin, X. Zhou, and K. Burke,

Restoring the density-gradient expansion for exchange in solids and surfaces, Phys. Rev. Lett. **100**, 136406 (2008).

[54] A. van de Walle, M. Asta, and G. Ceder, The alloy theoretic automated toolkit: A user guide, Calphad **26**, 539 (2002).

[55] V. Wang, N. Xu, J.-C. Liu, G. Tang, and W.-T. Geng, VASPKIT: A user-friendly interface facilitating high-throughput computing and analysis using VASP code, Comput. Phys. Commun. **267**, 108033 (2021).